AGU ADVANCING EARTH AND SPACE SCIENCES

JAMES | Journal of Advances in Modeling Earth Systems®

RESEARCH ARTICLE
10.1029/2024MS004300

Key Points:

- This study presents and evaluates a canopy wind model that simulates horizontal wind speeds above and within vegetation canopies
- Model results agree well with observations and should provide a better representation of wind flow in numerical weather prediction models
- The wind adjustment factor model provides midflame wind speed estimation, which can be used for the estimation of the rate of fire spread

Correspondence to:
W.-T. Hung,
wei-ting.hung@noaa.gov

Citation:
Hung, W.-T., Campbell, P. C., Moon, Z., Saylor, R., Kochendorfer, J., Lee, T. R., & Massman, W. (2024). Evaluation of an in-canopy wind and wind adjustment factor model for wildfire spread applications across scales. *Journal of Advances in Modeling Earth Systems*, *16*, e2024MS004300. https://doi.org/10.1029/2024MS004300

Received 20 FEB 2024
Accepted 11 JUN 2024

Evaluation of an In-Canopy Wind and Wind Adjustment Factor Model for Wildfire Spread Applications Across Scales

Wei-Ting Hung[1,2], Patrick C. Campbell[1,2], Zachary Moon[2,3], Rick Saylor[2], John Kochendorfer[2], Temple R. Lee[2], and William Massman[4]

[1]Cooperative Institute for Satellite Earth System Studies, Center for Spatial Information Science and Systems, George Mason University, Fairfax, VA, USA, [2]Air Resources Laboratory, National Oceanic and Atmospheric Administration, College Park, MD, USA, [3]Earth Resources Technology, Inc., Laurel, MD, USA, [4]U.S. Department of Agriculture Forest Service, Rocky Mountain Research Station, Fort Collins, CO, USA

Abstract The representation of vegetative sub-canopy wind is critical in numerical weather prediction (NWP) models for the determination of the air-surface exchange processes of heat, momentum, and trace gases. Because of the relationship between wind speed and fire behaviors, the influence of the canopy on near-surface wind speed is critical for prognostic fire spread models used in regional NWP models. In practice, the wind speed at the midflame point of fires (midflame wind speed) is used to determine the rate of fire spread. However, the wind speeds from most in situ measurements and NWP models are taken at some reference height above the canopy and fire flames. Hence, this study develops a modular and computationally-efficient one-dimensional model set composed of a canopy wind model and a wind adjustment factor (WAF) model for NWP applications across scales. The model set uses prescribed foliage shape functions to represent the vertical vegetation profile and its impacts on the three-dimensional structure of horizontal wind speeds. Results from the canopy wind model well agree with ground-based observations with average mean absolute bias, root mean square error and determination coefficients around 0.18 m s^{-1}, 0.40 m s^{-1} and 0.90, respectively. The WAF model provides midflame wind speeds by estimating the WAF based on canopy, fire and flame characteristics. Various user-definable options provide flexibility to adapt to variations in canopy characteristics and additional complexities associated with wildfires. The model set is expected to improve NWP models by providing an improved representation of the sub-grid wind flows at any spatial scale.

Plain Language Summary Compared to bare ground, wind speeds are reduced by the presence of vegetation at the surface by the leaves and woody parts of plants, especially within forest canopies. The altered wind speeds affect the atmosphere's stability and transport processes, as well as the spread of wildfires. Several fire prediction models are connected with weather models; however, most weather models do not consider such sub-canopy effects on reducing wind speeds as the vertical structure of vegetation are not included in the models. Thus, this study presents a canopy model that can simulate the effects of vegetation, primarily forest canopies, on horizontal wind speeds used in weather models. The canopy model also provides the estimation of the wind speeds at the height of the midpoint of flame above ground level (midflame wind speed), which can better describe fire behaviors for general use in fire prediction models. The model results agree well with both above and below canopy top wind speed observations, and the midflame wind speeds are reliable when compared to previous studies. The canopy model is expected to improve weather modeling by providing a better representation of near-surface wind flow, particularly for areas covered by dense forest canopies.

1. Introduction

Winds in the boundary layer are strongly affected by vegetative canopies, especially regions of contiguous forests. Due to the drag forces introduced by leaves and branches, horizontal wind speeds are reduced near and within the canopy compared to the airflow above bare soil (Chen et al., 1993; Grimmond et al., 2000; Raupach, 1991; Thom, 1971). The presence of vegetation increases turbulence near and within the canopy and influences atmospheric stability and the vertical exchanges of momentum, heat and water vapor (Poggi et al., 2004; Raupach & Thom, 1981; Raupach et al., 1996). Moreover, the altered wind speeds can affect atmospheric composition by modulating the dispersion and deposition rate of air components (Freire et al., 2017; Lamaud et al., 2002; Makar et al., 2017). Since over 80% of the land on the Earth is covered by vegetation and nearly 30% is covered by forests (Potapov et al., 2022), it is important for regional-to global-scale climate and numerical weather prediction (NWP) models, including coupled prognostic models, to have an accurate representation of the land surface and more explicitly defined in-canopy wind speeds.

However, most NWP models assume a single layer of combined vegetation and soil (the "big-leaf " approach) in the coupled land surface models. For instance, vegetation is treated as part of the surface roughness and is not vertically resolved in the Noah land surface model (Ek et al., 2003) that is widely used in the Weather Research and Forecast (WRF) model (Skamarock et al., 2019). The near-surface wind speeds in NWP models are derived from the wind speeds at the lowest model layer by assuming a logarithmic wind profile based on the Monin-Obukhov similarity theory (MOST; Monin & Obukhov, 1954). In MOST, the ground is referred to the surface roughness, which is the combination of vegetative canopy and bare soil, and wind speeds go to zeros at the height of surface roughness (i.e., roughness length of the soil ground plus displacement height due to vegetation). In this case, wind speeds at a given height above the ground are referred to a given height above the vegetative canopy, and in-canopy wind speeds are usually not available in NWP models.

The lack of explicit in-canopy wind speeds in NWP models may not only affect the simulations for the transport and deposition of air pollutants, but also for the emissions of various trace gases and aerosols. Wildfires emit large amounts of aerosol and trace gases into the atmosphere (Andreae & Merlet, 2001; Crutzen & Andreae, 1990; Kaulfus et al., 2017; Reid et al., 2005), and wildfires can be the main source of air pollutants in certain regions and seasons. Fire emissions in nature are highly dependent on fire behavior (e.g., spread, duration and intensity) and flame characteristics (e.g., flame height, length, and angle), which are highly sensitive to the underlying canopy effects on winds (Liu et al., 2021). According to field measurements and laboratory experiments, fire spread is linearly correlated with wind speeds (Beer, 1993; Cheney & Gould, 1995; Cheney et al., 1993, 1998; Rothermel, 1972).

Most state-of-the-science prognostic fire spread models used in NWP models, such as the fire behavior module in the WRF model (WRF-FIRE; Coen et al., 2013), SPread and InTensity of FIRE model (SPITFIRE; Thonicke et al., 2010) and the Region-Specific ecosystem feedback Fire model (RESFire; Zou et al., 2019), are built based on Rothermel's surface fire spread model (Rothermel, 1972). In Rothermel's model, wind speeds at the midflame point (i.e., the midpoint of fire flame above the ground) are used to better describe the influence of wind speeds on the spread of fires. In practice, most wind measurements and NWP models provide wind speeds at a height of 10 m above the vegetative canopy surface, which is usually much higher than fire flames. Thus, often a constant scale factor is used to bring wind speeds from a reference height above the canopy (e.g. 10 m) down to the midpoint of the flames (Andrews, 2012; Lawrence et al., 2019; Thonicke et al., 2010). However, the influence of vegetative canopy is still not properly considered in such an approach since the vertical structure of canopy is not resolved in NWP models. Hence, the application and evaluation of in-canopy wind speeds and the estimation of the scale factor (hereafter referred to as the wind adjustment factor (WAF) adopted from Andrews (2012)) are important to NWP models as well as to coupled prognostic fire spread models of wildfire spread and resulting emissions, and such applications need to be evaluated for their practical usage. Mallia et al. (2020) found that the application of in-canopy wind speeds and WAF improved the simulation of fire growth, heat release and smoke dispersion by conducting a comprehensive investigation on fire behaviors and smoke plume rise, but their study only focused on a prescribed burning case over the western Florida in the early November of 2012. Therefore, a set of generalized and comprehensive formulations of in-canopy wind speed, flame height and WAF for cross-scale NWP model applications remains lacking.

In this study, a modular one-dimensional model set composed of canopy wind and WAF components for regional- and global-scale NWP applications (referred to as the "canopy wind model" and the "WAF model", respectively) is developed based on Massman et al. (2017). The canopy wind model is comprehensively evaluated against a suite of flux tower above and within canopy wind observations, and the WAF model is evaluated against a previous study for a historical fire case in 2018 to assess the derived WAF. Massman et al. (2017) provides an in-canopy wind model that includes a self-consistent set of canopy wind speed and WAF formulations based on prescribed foliage distribution shape functions allowing for a generalized application to various canopy types. Furthermore, the simple analytical expressions for in-canopy wind speeds allow the models to run with minimal computational cost, which is advantageous to already computationally expensive NWP models. As an extension, the goal of this study is to create a canopy model set that can not only be used as a stand-alone application but also be coupled with NWP models as an online model component. This manuscript is structured as follows. A brief description of the canopy wind and WAF models, including adaptations of Massman et al. (2017), is given in

Section 2. Evaluation of in-canopy wind speed by comparing against flux tower observations and sensitivity of the performance of in-canopy wind speed simulation are discussed in Section 3. A comprehensive assessment of the applications to regional NWP models of the canopy wind and WAF models, including examples of gridded in-canopy wind speeds and evaluation of WAF estimation, is provided in Section 4. Possible sources of model uncertainties and limitations are discussed in Section 5, with overall study conclusions in Section 6.

2. Model Description

2.1. In-Canopy Wind Model

Following Massman et al. (2017) (hereafter referred to as "M17"), the calculation of in-canopy wind speed includes two basic steps: (a) estimation of the canopy density profile from prescribed foliage shape functions and (b) estimation of the wind profiles in the top and bottom portions of the canopy. First, the canopy density profile, $h_a(\xi)$, is defined as the product of total plant density (i.e., plant area index, PAI) and canopy density fraction (i.e., fraction of bottom-up canopy density to total canopy density, $FRAC(\xi)$):

$$h_a(\xi) = PAI \times FRAC(\xi) = PAI \times \frac{f_a(\xi)}{\int_0^1 f_a(\xi')\, d\xi'} \tag{1}$$

where ξ is the ratio of height of the level above ground (z) to height of the canopy top (canopy height, h), $f_a(\xi)$ is the foliage distribution shape function, and $\int_0^1 f_a(\xi')\, d\xi'$ is the integration of $f_a(\xi)$ from the surface ($\xi = 0$) to the canopy top ($\xi = 1$). The nondimensional term ξ allows the model to calculate the wind speed at any desired level within the canopy independently, regardless of canopy type and structure. The mathematical expression of $f_a(\xi)$ is shown below:

$$f_a(\xi) = \begin{cases} \exp\left(\dfrac{-(\xi - \xi_{max})^2}{\sigma_u^2}\right), & \xi_{max} \le \xi \le 1 \\[2ex] \exp\left(\dfrac{-(\xi_{max} - \xi)^2}{\sigma_1^2}\right), & 0 \le \xi \le \xi_{max} \end{cases} \tag{2}$$

where ξ_{max} is the height of the maximum plant density, and σ_u and σ_1 are standard deviations of plant density above and below ξ_{max}, respectively. This form for the foliage distribution shape function is chosen for its simplicity, generality, and computational efficiency. The three required parameters that describe the foliage shape function (ξ_{max}, σ_u and σ_1) are determined based on the specific canopy type.

The approach used in M17 parameterizes $f_a(\xi)$ for eight canopy types, including aspen, jack pine, scots pine, loblolloy pine, hardwood, corn, spruce, and rice, whereas the canopy wind model for regional to global scale NWP applications must reclassify and/or simplify these canopy types into four grouped categories: evergreen forest, deciduous forest, mixed forest, and generally low-lying vegetation. Mixed forest is defined as a combination of evergreen and deciduous forests. Low-lying vegetation includes grasslands and croplands by assuming they share a similar foliage shape (Bonan et al., 2018). Shrublands are classified as mixed forest as they often have a tree-like foliage density distribution. Note that the classifications of grasslands and shrublands are simplified approaches following the canopy types reported in M17 and could result in potential uncertainties, as grasslands and shrublands may have different foliage density shapes from croplands and forests, respectively. The reclassifications are based on the annual surface type (AST; Huang et al., 2022) product from the Visible Infrared Imaging Radiometer Suite (VIIRS) sensor onboard the Suomi National Polar orbiting Partnership (SNPP) satellite, which follows the International Geosphere-Biosphere Programme (IGBP) land cover classification that is commonly used in regional/global scale NWP models. Figure 1 visualizes the $f_a(\xi)$ of four canopy categories used in the canopy wind model, and Table 1 provides the $f_a(\xi)$ parameter values for each canopy category with its corresponding VIIRS AST. The parameters are calculated by averaging the parameters of all associated canopy types in the M17 model. For instance, the parameters for evergreen forest in the canopy wind model are the average of those for spruce and pines in M17. Note that the parameters for low-lying vegetation are based on crops (corn and rice) and may introduce potential uncertainties for grasslands.

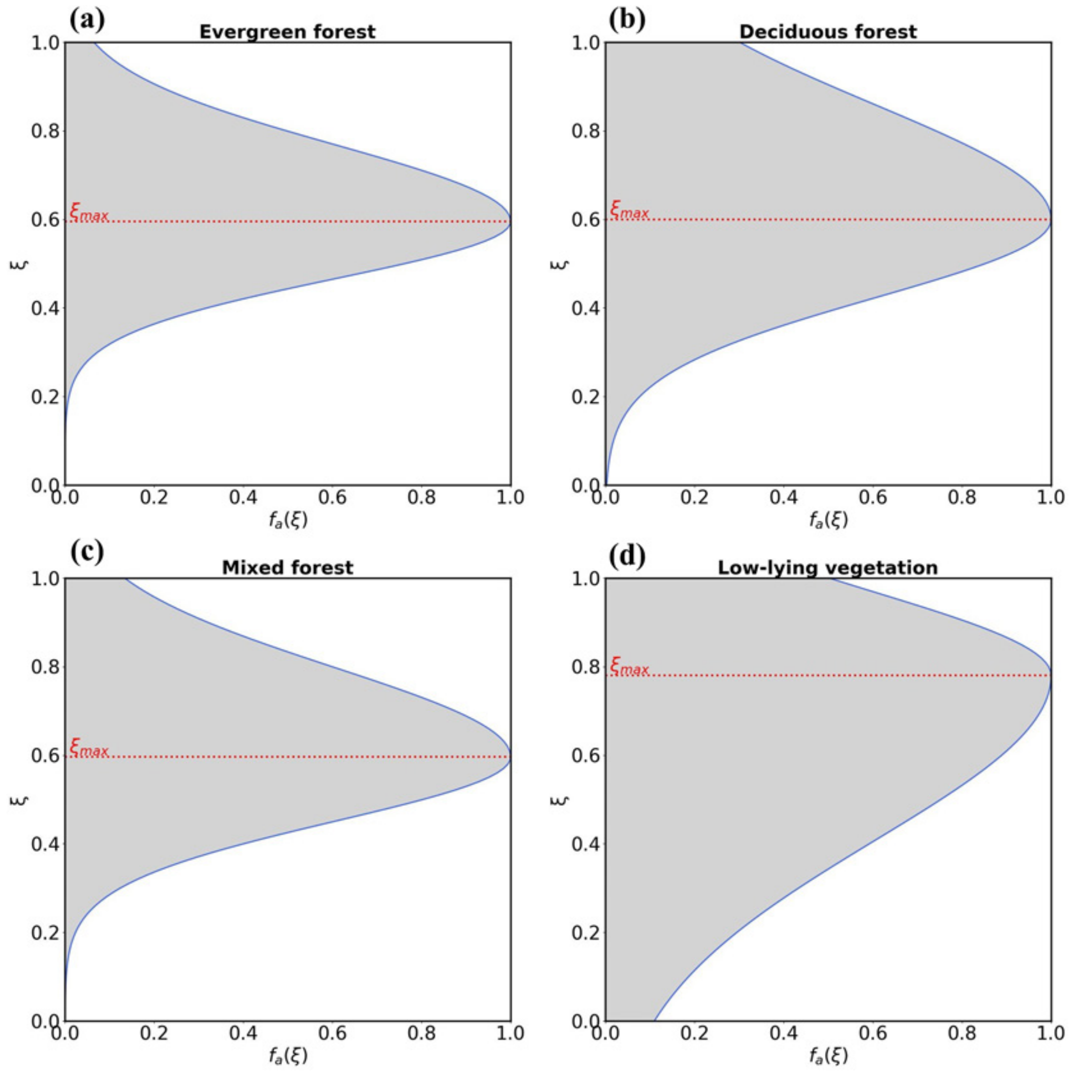

Figure 1. Foliage distribution shape function $f_a(\xi)$ for (a) evergreen forest, (b) deciduous forest, (c) mixed forest, and (d) low-lying vegetations used in the canopy wind model. The associated parameter values are adapted from M17 and shown in Table 1.

Two terms are required to calculate the in-canopy wind speed. The first term $U_b(\xi)$ describes the logarithmic reduction of wind speed that dominates within the lower part of the canopy:

$$U_b(\xi) = \begin{cases} \dfrac{\log(z/z_0)}{\log(h/z_0)} = \dfrac{\log\left(\xi/\xi_{z0}\right)}{\log\left(1/\xi_{z0}\right)}, & z_0 \le z \le h \\ 0, & 0 \le z \le z_0 \end{cases} \tag{3}$$

Table 1
Parameter Values of Four Canopy Categories Used in Equations 2 and 5 With Corresponding VIIRS AST

Canopy type in the present model	ξ_{max}	σ_u	σ_1	C_d	VIIRS AST	Canopy type in the M17 model
Evergreen forest	0.60	0.25	0.18	0.21	1, 2	Spruce, Jack pine, scots pine, loblolloy pine
Deciduous forest	0.60	0.37	0.25	0.18	3, 4	Aspen, hardwood
Mixed forest	0.60	0.29	0.21	0.20	5, 6, 7	Spruce, Jack pine, scots pine, loblolloy pine, Aspen, hardwood
Low-lying vegetation	0.780	0.265	0.525	0.300	8, 9, 10, 12	Corn, rice

Note. The parameter values are calculated as the averages of the values of corresponding canopy types in M17.

where z_0 is the surface (i.e., bare soil) roughness length of the ground, and ξ_{z0} is the ratio of surface roughness length to the canopy height (i.e., $\xi_{z0} = z_0/h$). Following M17, $\xi_{z0} = 0.0025$ is used in the in-canopy wind speed calculation in the canopy wind model by default. It is worth noting that this equation satisfies the no-slip lower boundary condition, by reducing the wind speed to zero at the height of the surface roughness length to better simulate a realistic vertical wind speed profile.

The second term $U_t(\xi)$ describes the reduction effects of vegetation on the wind speed near the upper part of the canopy, which is dominated by drag effects:

$$U_t(\xi) = \frac{cosh\,(N \times FRAC_d(\xi))}{cosh\,(N)}, \qquad 0 \leq \xi \leq 1 \tag{4}$$

where N is defined as the ratio of the total drag area ($DRAG$) to the canopy stress ($CSTRESS$):

$$N = \frac{DRAG}{CSTRESS} = \frac{C_d \times PAI}{2u_c^{*2}/u_c^2} \tag{5}$$

where C_d is the drag area coefficient adapted from M17 (Table 1), u_c^* is the friction velocity at the canopy top, u_c is the wind speed at the canopy top, and $FRAC_d(\xi)$ is the fraction of the bottom-up integrated drag area to the total drag area of the canopy. In the canopy wind model, the drag effect is assumed to be independent from the winds and is dominated by canopy density. Thus, $FRAC_d(\xi)$ is approximately equal to $FRAC(\xi)$, and $U_t(\xi)$ can be expressed as:

$$U_t(\xi) = \frac{cosh\,(N \times FRAC(\xi))}{cosh\,(N)}, \qquad 0 \leq \xi \leq 1 \tag{6}$$

The ratio u_c^*/u_c is calculated as:

$$\frac{u_c^*}{u_c} = c_1 - c_2\, exp\,(-c_3 \times DRAG) \tag{7}$$

where $c_1 = 0.38$, $c_2 = c_1 + \frac{k}{log\,(\xi_{z0})}$ assuming a von Karman constant $k = 0.4$, and $c_3 = 15$.

Finally, the in-canopy wind profile $u(\xi)$ can be expressed as the product of the two terms and the wind speed at canopy top (u_c):

$$u(\xi) = U_b(\xi)\, U_t(\xi)\; u_c, \qquad 0 \leq \xi \leq 1 \tag{8}$$

2.2. Estimation of the Above-Canopy Wind Profile and Wind Speed at the Canopy Top

The estimation of u_c is a critical task in terms of the $u(\xi)$ calculation, since most in situ measurements and NWP models provide wind speeds at some height well above the canopy. The distance between the height of the above-canopy winds and the canopy top is defined as the reference height (e.g., reference height = 10 m for 10 m above the canopy top). To calculate the winds at and above the canopy top, the canopy wind model adapts a variant of the above-canopy log-wind speed profile from the community Noah land surface model with multiparameterization options (Noah-MP) (He et al., 2023; Niu et al., 2011; https://github.com/NCAR/noahmp). The parameterization is based on MOST and adjusted here to approximately account for the surface roughness sublayer (RSL) effects above the canopy:

$$u(z) = u_{ref} \times \frac{ln(\lambda_{rs}(z - d + z_0)/z_0)}{ln(h_{ref}/z_0)}, \qquad z \geq h \tag{9}$$

where $u(z)$ is the wind speed at level z above the ground, h_{ref} is the reference height, u_{ref} is the wind speed at the reference height above the canopy (reference wind speed), $\lambda_{rs} = 1.25$ is adopted as the influence function associated with the RSL effects in the M17 model, d is the zero-plane displacement height, and z_0 is the surface (soil) roughness length. The limitation of z (i.e., $z \geq h$) restricts $u(z)$ to be applicable to the wind speeds above the canopy only. The log-wind profile formulation (Equation 9) is used as it is readily applied in NWP models and applicable to combine with M17 in the approach described here. It is important to note that this formulation is assumed to be under neutrally buoyant conditions based on MOST. Also, the use of λ_{rs} to represent the RSL effects in the canopy wind model is a simplification, as the RSL effects vary with diabatic stability, wind speeds and canopy characteristics (Abolafia-Rosenzweig et al., 2021).

Initial estimates for the NWP resolved z_0 and d are first made in the canopy wind model. The first-estimate z_0 is taken from user input, while the d is initially estimated as $0.75 \times h$ (canopy height) which is the typical approximation in NWP models (Martano, 2000; Stull, 1988). The initial estimates are used to approximate u_c and u_c^* calculations based on Equations 7 and 10, respectively. Afterward, d and z_0 are recalculated following M17 (see Appendix 1 for details) and the revised values are used for final u_c and in-canopy wind estimations. This is a critical step as it closes the set of equations in the M17 model and takes into account the RSL and drag effects on the final calculations of d and z_0.

Finally, $u(z) = u_c$ when z equals canopy height (i.e., $z = h$):

$$u_c = u_{ref} \times \frac{ln(\lambda_{rs}(h - d + z_0)/z_0)}{ln(h_{ref}/z_0)} \tag{10}$$

This function directly brings the wind speed at the reference height to the canopy top, providing a robust estimation of u_c.

2.3. Wind Adjustment Factor

The WAF model adopts the WAF calculation from M17, which is defined as the ratio of the midflame wind speed (u_{mid}) to the reference wind speed (u_{ref}) at the reference height above the canopy top (h_{ref}; 10 m by default). In a simplified approach for regional and global NWP applications, u_{mid} is dependent on the height of the midflame point and canopy type only.

The height of the midflame point (h_{mid}) is simply defined as the one-half of the flame height (h_{flame}) above ground level:

$$h_{mid} = \frac{1}{2} \times h_{flame} \tag{11}$$

However, definition of a gross flame height is difficult under this context of wildfires in regional to global NWP systems, and such flame dimensions (including flame length and angle) are affected by multiple factors including the overall ambient conditions, topographic characteristics, canopy structure, and more detailed plant trait information such as fuel type/load, age, stress, and moisture content. These canopy-associated factors are further modulated by the fire environment, and thus result in complex relationships that can only be more comprehensively modeled using mechanistic and computationally expensive fire behavior models (e.g., Zylstra, 2021). To simplify the calculation for cross-scale NWP applications, the WAF model assumes that the flame height is equal to the flame length (L) (i.e., under calm winds), such that the h_{flame} may be approximated using only fire intensity following Byram (1959) and Alexander (1982):

$$h_{flame} = L = \alpha \times I^{\beta} \tag{12}$$

α and β are fuel type and fire behavior dependent constants based on Alexander and Cruz (2012), which are summarized in Table 2. To account for the variability of the relationship between fire height and fire intensity, multiple formulations from various references are used for each vegetation type. The final estimate of h_{flame} is calculated as the average of the results of corresponding formulations using Equation 12 with associated α and β. For example, the final estimate of h_{flame} for evergreen forest is calculated as the average of the h_{flame} results derived from Equation 12 using each of the six α and β in Table 2.

Table 2
Relevant Constants Used for Flame Height Calculation (Equation 12)

Vegetation type	VIIRS AST	α	β	Fuel/Fire type	Reference
Evergreen forest	1, 2	0.0775	0.460	Pine litter with grass understory	Byram (1959)
		0.074	0.651	Lodgepole pine slash	Anderson et al. (1966)
		0.0447	0.670	Douglas-fir slash	
		0.0147	0.767	Eucalypt forest	Burrows (1994)
		0.045	0.543	Maritime pine (head fire)	Fernandes et al. (2009)
		0.029	0.724	Maritime pine (backfire)	
Deciduous forest	3, 4	0.0377	0.500	Southern US	Nelson (1980)
		0.016	0.700	Excelsior	Weise and Biging (1996)
Mixed forest	5	0.0377	0.500	Southern US	Nelson (1980)
Low-lying vegetation: Shrubland	6, 7	0.475	0.493	Litter and shrublands	Nelson and Adkins (1986)
		0.0075	0.460	Fynbos shrublands	van Wilgen (1986)
		0.087	0.493	Shrublands	Vega et al. (1998)
		0.0325	0.560	Shrublands	Catchpole et al. (1998)
		0.0516	0.453	Shrublands	Fernandes et al. (2000)
Low-lying vegetation: Grassland and cropland	8, 9, 10, 12	0.0775	0.460	Pine litter with grass understory	Byram (1959)
		0.00015	1.750	Grasslands (head fire)	Clark (1983)
		0.000722	0.990	Grasslands (backfire)	

In Equation 12, I is the fire intensity over a linear distance, which here is estimated using fire radiative power (FRP) from satellite observations across a given model grid resolution (dx):

$$I = \frac{FRP}{dx} \tag{13}$$

Satellite FRP is commonly used as an input of the prognostic fire spread models in operational NWP models, such as the High Resolution Rapid Refresh for Smoke (HRRR-Smoke; Ahmadov et al., 2017) and the Aerosol Forecast Member in the Global Ensemble Forecast System (GEFS-Aerosols; Zhang et al., 2022), to determine the fire location and intensity in near real time. The linkage of I and FRP provides the WAF model a simple and efficient manner to calculate WAF for NWP models across scales.

The model grid-cell vegetation/canopy type based on VIIRS AST is used as a binary determination for whether the fires are above or below the canopy, and further affect the estimation of u_{mid}. Following M17, fires that occur within tall and dense canopies such as forests are assumed to be sub-canopy fires, and thus the midflame wind speed is affected by both the wind reduction within the canopy and the MOST + RSL effects in the region between the reference height above the canopy and the canopy top. The WAF for sub-canopy fires can be expressed following M17 as:

$$WAF = u(\xi_{mid}) \times \frac{u_c}{u_{ref}} = U_b(\xi_{mid})\, U_t(\xi_{mid}) \times \frac{ln\left(\lambda_{rs} \frac{1-d/h}{z_0/h}\right)}{ln\left(\lambda_{rs} \frac{h_{ref}/h+1-d/h}{z_0/h}\right)} \tag{14}$$

where ξ_{mid} is the ratio of the midflame height to the canopy height (i.e., $\xi_{mid} = h_{mid}/h$), d is the zero-plane displacement height, z_0 is surface roughness length, and h_{ref} is the reference height. The definitions of d/h and z_0/h, which are functions of canopy height, friction velocity and canopy stress, can be found in Appendix 1.

Fires that occur in short vegetation such as grass and crops are assumed to be above-canopy fires, where the flames typically extend higher than the canopy top. In this case, the midflame wind speed is mainly affected by the wind reduction due to the MOST + RSL effect above the canopy top, and is therefore defined as the average over

10.1029/2024MS004300

the flame above the canopy top (i.e., between h and $h + h_{flame}$). The WAF for above-canopy fires can be expressed as:

$$WAF = \frac{\frac{1}{h_{flame}}\int_{h}^{h+h_{flame}} u(z)\,dz}{u_{ref}} = \frac{\ln\left(\lambda_{rs}\frac{h_{flame}/h+1-d/h}{z_0/h}\right) - 1 + \delta \times \ln\left(\frac{1}{\delta}+1\right)}{\ln\left(\lambda_{rs}\frac{h_{ref}/h+1-d/h}{z_0/h}\right)} \tag{15}$$

with

$$\delta = \frac{1 - d/h}{h_{flame}/h} \tag{16}$$

Detailed definitions of each factor and discussion about the sensitivities of WAF can be found in M17.

2.4. Model Configurations

The canopy model set (i.e., the canopy wind and WAF models) has a user-defined vertical resolution (above and below canopy), which uses 100 vertical layers from the surface to 50 m above ground level with an interval of 0.5 m by default. Vegetation-type dependent PAI look-up tables from Katul et al. (2004) are used for PAI estimation by default; however, PAI parameterizations based on Equation 19 from M17, leaf area index (LAI) that could be retrieved from either model products or observations, and user-defined, spatially-constant PAI options are also available. Equation 19 from M17 formulates PAI as a function of canopy height, canopy cover and crown ratio, while canopy cover is assumed to be canopy fraction, and crown ratio is calculated as one-third of canopy fraction according to Andrews (2012) in the canopy wind model. Furthermore, when LAI is provided as input to the canopy wind model, PAI can be determined by following the PAI-LAI relationship based on a combination of Equations 10 and 14 from Zou et al. (2009):

$$\mathrm{PAI} = \mathrm{LAI}/(1 - \alpha) \tag{17}$$

where α is the woody-to-total area ratio that describes the contribution of woody components to the total area of plant. Typically, a plant is considered as a combination of leafy and woody components (Chen & Cihlar, 1995; Kucharik et al., 1998; Li et al., 2018; Olivas et al., 2013; Zou et al., 2009), and thus $1 - \alpha$ describes the contribution of leafy components to the total area of plant. In the canopy wind model, α is vegetation type dependent and is determined based on previous studies (Chen et al., 1997; Fang et al., 2019; Gower et al., 1999; Kucharik et al., 1998).

Moreover, the canopy wind and WAF models are able to use both one-dimensional single location data and two-dimensional gridded data sets over any given domain as inputs. In the latter case, the models identify the presence of vegetation (canopy grids) based on user-defined thresholds of canopy height, canopy fraction, and LAI. More details are given in Section 4.

The required input variables for the in-canopy wind and WAF calculations in the canopy wind and WAF models are summarized in Table 3. In this study, the climatological forest height of 2020 derived from the global ecosystem dynamics investigation (GEDI) measurements blended with Landsat archive data (Potapov et al., 2020) is used as forest canopy height. The 2020 climatological forest fraction is from the moderate resolution imaging spectroradiometer collection 6.1 (MODISv061) (DiMiceli et al., 2022), and the 2020 monthly average of LAI is from the VIIRS vegetation health product (VHP; Myneni & Knyazikhin, 2018). Since this study primarily focuses on forest canopy, GEDI forest height and MODIS forest fraction are used as the proxy of canopy height and canopy fraction, respectively. For model evaluation, the reference wind speed is from the wind measurements at selected ground-based sites. For the assessment of gridded data and NWP model application, the reference wind speed is based on the horizontal wind speeds at 10 m above the surface from the High-Resolution Rapid Refresh version 3 (HRRRv3; Alexander et al., 2010; https://rapidrefresh.noaa.gov/hrrr/). HRRR is an operational atmospheric model at the National Oceanic and Atmospheric Administration (NOAA) National Centers for Environmental Prediction (NCEP), providing near-real-time hourly weather forecasts for the United States. The surface roughness length (z_0), which is used as the initial first guess in u_c calculation, is also from

Table 3
List of Input Variables of the Canopy Wind and Wind Adjustment Factor Models and Data Sets Used in This Study

Variable	Data source
Latitude (degree)	-
Longitude (degree)	-
Time	-
Canopy height (m)	GLAD[a]
Reference wind speed (m s^{-1})	Ameriflux[b], GOA[c], HRRRv3[d]
Vegetation type (dimensionless)	VIIRS AST[e]
Leaf area index (m^2 m^{-2})	VIIRS VNP[f]
Reference height (m)	Ameriflux, GOA
Canopy fraction (dimensionless)	MODIS v061[g]
Surface roughness length (m)	HRRRv3
Fire radiative power (MW)	RAVE[h]

Note. Note that fire radiative power is used for WAF calculation only. [a]https://glad.umd.edu/dataset/GLCLUC2020. [b]https://ameriflux.lbl.gov/. [c]https://www.arm.gov/research/campaigns/amf2014goamazon. [d]https://rapidrefresh.noaa.gov/hrrr/; https://home.chpc.utah.edu/~u0553130/Brian_Blaylock/cgi-bin/hrrr_download.cgi. [e]https://www.star.nesdis.noaa.gov/jpss/st.php. [f]https://lpdaac.usgs.gov/products/vnp15a2hv001/. [g]https://lpdaac.usgs.gov/products/mod44bv061/. [h]https://sites.google.com/view/rave-emission/.

HRRRv3. FRP from the Regional advanced baseline imager (ABI) and VIIRS fire Emissions (RAVE; Li et al., 2022) is used for WAF estimation. RAVE is a fire emission inventory that provides hourly FRP and fire emissions with a spatial resolution of 3 km. RAVE products are based on the ABI onboard the Geostationary Operational Environmental Satellite *R* Series (GOES-R), and the VIIRS sensors onboard SNPP and Joint Polar Satellite System (JPSS) satellites. Detail of each data set can be found in cited references.

3. Model Evaluation

The canopy wind model is evaluated by comparing simulated wind profiles with horizontal wind speed measurements deployed on flux towers. Ameriflux is a network of ground-based flux sites covering major vegetation canopies such as forest, savanna, and grassland in North and South America. Wind speed measurements from four operational Ameriflux sites across the contiguous United States (CONUS) that contain at least three measurements within the canopy and have continuous observations for at least one summer season are used, including Willow Creek (US-WCr), Bartlett Experimental Forest (US-xBR), Chestnut Ridge (US-Chr) and Lower Teakettle (US-xTE) sites. Additionally, in-canopy wind speeds are evaluated against observations from a fifth site taken from the Green Ocean Amazon (GOA) field campaign (Freire et al., 2017; Fuentes et al., 2016; Santos et al., 2016). GOA was performed at a research site located in the Amazon rainforest in the Cuieiras Biological Reserve, Brazil. The continuous wind speed observations at multiple levels within the canopy at GOA makes it an ideal site for in-canopy wind evaluation. The information for and locations of selected sites are shown in Table 4 and Figure 2. The wind speeds at selected sites are measured by sonic anemometers (model CSAT3, Campbell Scientific, Inc. and model Young-81000, Young) with offset error less than ±0.08 m s^{-1} (https://www.campbellsci.com/csat3 and https://www.youngusa.com/product/ultrasonic-anemometer/).

For Ameriflux sites, consistent summer seasons are used to minimize the influence of the seasonal variations of PAI. As for the GOA site, a full-year period is used by assuming a less variable climate and relatively minimal PAI seasonal variations in tropical regions throughout the year compared with the Ameriflux sites. The wind profiles with wind speeds equal to zero at all sites and the wind profiles with outliers (i.e., mean plus three times of standard deviation, which is ~5.8 m s^{-1}) at GOA site are omitted from the analysis. Hourly wind profiles at 1800 UTC (1,100–1400 LT) and 0600 UTC (2300–0200 LT) are used to represent daytime and nighttime wind profiles, respectively. The reference wind speed, reference height, canopy height, and vegetation type are determined based on site characteristics, while initial surface roughness length is taken as that used for the site's location in

Table 4
List of Selected Horizontal Wind Tower Sites

Site name	Time zone	Lon, lat (degree)	Vegetation type	Canopy height (m)	Measurement height (m)	Time period
Willow creek, WI (US-WCr)	UTC-5	−90.08, 40.81	Mixed forest	24.3	12.20, 18.30, 24.40*, 29.60**	1 June–30 September 2016
Bartlett experimental forest, NH (US-xBR)	UTC-4	−71.29, 44.06	Mixed forest	23.0	0.56, 2.48, 15.50, 19.20, 25.48*, 35.68**	1 June–30 September 2019
Chestnut ridge, TN (US-Chr)	UTC-5	−84.33, 35.93	Mixed forest	25.0	5, 10, 15, 20, 25*, 30**, 35, 40, 45, 50	30 May–11 September 2018
Lower teakettle, CA (US-xTE)	UTC-6	−119.01, 37.00	Evergreen forest	32.0	0.29, 2.79, 9.48, 18.01, 26.22, 32.08*, 58.71**	1 June 1–30 September 2020
Green Ocean Amazon (GOA)	UTC-4	−60.21, −2.60	Mixed forest	35.0	1.40, 7.00, 13.65, 18.20, 22.05, 24.50, 31.50, 35.00*, 40.25**, 48.30	23 Mar 2014–16 January 2015

Note. The measurement heights closest to the canopy top and at the first level above the canopy at each site are marked with asterisks and double-asterisks, respectively.

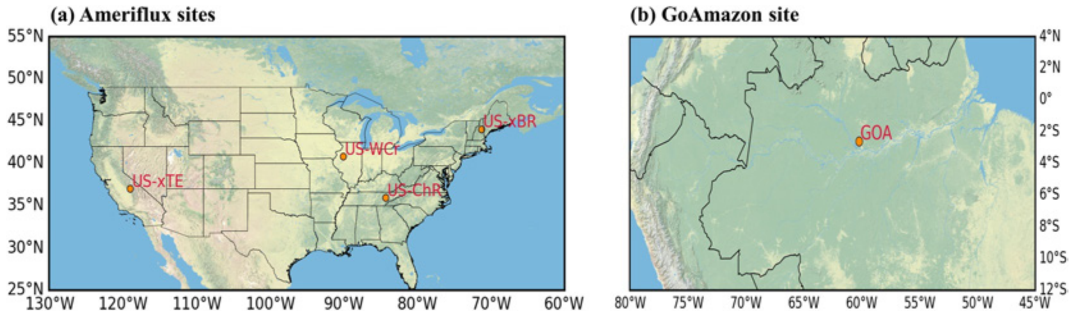

Figure 2. Location of (a) Ameriflux sites and (b) GoAmazon site.

HRRRv3 and friction velocity is calculated by the canopy wind model (Equation 7). Note that the canopy height (24.3 m) and measurement height (24.4 m) at US-WCr site are adjusted to 24.5 m, and the measurement height (32.08 m) at US-xTE site is adjusted to 32.0 m to fit to the model resolution (0.5 m).

Three sets of model simulations are evaluated, and are summarized in Table 5. First, the wind profiles from the surface to the maximum model level (i.e. 50 m) (hereafter referred to as the "full wind profile") at selected sites are analyzed to evaluate the overall performance of the canopy wind model. Wind speeds at the reference heights (h_{ref}), which are determined based on the measurement height at each site, are used as the reference wind speeds (u_{ref}). Here the contributions from both the MOST + RSL effects above the canopy top and foliage density below the canopy top are considered. While the measurement heights vary with sites, the maximum measurement level may extend above the model layers at some sites. Second, the wind profiles within the canopy (in-canopy wind profile) at selected sites are analyzed by using the wind speeds at the canopy top ($h_{ref} = 0$) as the reference wind speeds with a focus on the evaluation of the foliage effects on wind speeds. Third, multiple in-canopy wind profiles with different PAI options, vegetation type settings and model vertical resolution configurations at US-xTE site are compared for model sensitivity test.

3.1. Full Wind Profile Comparison

Evaluation of wind profiles from the surface to the maximum model level (i.e. 50 m), including both in-canopy and above-canopy winds, are discussed in this section. The wind speed measurements at the first level above the canopy at selected sites are used as the reference winds (u_{ref}). Different reference heights (h_{ref}) are applied as the measurement heights vary by site, and the selected measurement heights at each site are marked with double-asterisks in Table 4. Figure 3 shows the observed wind profiles, comparisons of the mean wind profiles of model results and observations, and scatter plots of observed and model wind speeds at selected sites. Note that the maximum

Table 5
List of the Evaluation Sets

Evaluation set	Selected site	Time	Description
Full wind profile	US-WCr US-xBR US-Chr US-xTE GOA	0600 and 1800 UTC	Wind speeds at the reference heights (h_{ref}), which are determined based on the measurement height at each site, are used as the reference wind speeds (u_{ref}). Both the MOST + RSL effects above the canopy top and foliage density below the canopy top are considered.
In-canopy wind profile	US-WCr US-Chr US-xTE GOA	0600 and 1800 UTC	Wind speeds at the canopy top ($h_{ref} = 0$) are used as the reference winds (u_{ref}) to focus on the contribution of foliage effects within the canopy.
Model sensitivity test	US-xTE	0600 UTC	In-canopy wind profiles using six PAI options, four vegetation types and four model layer configurations are compared.

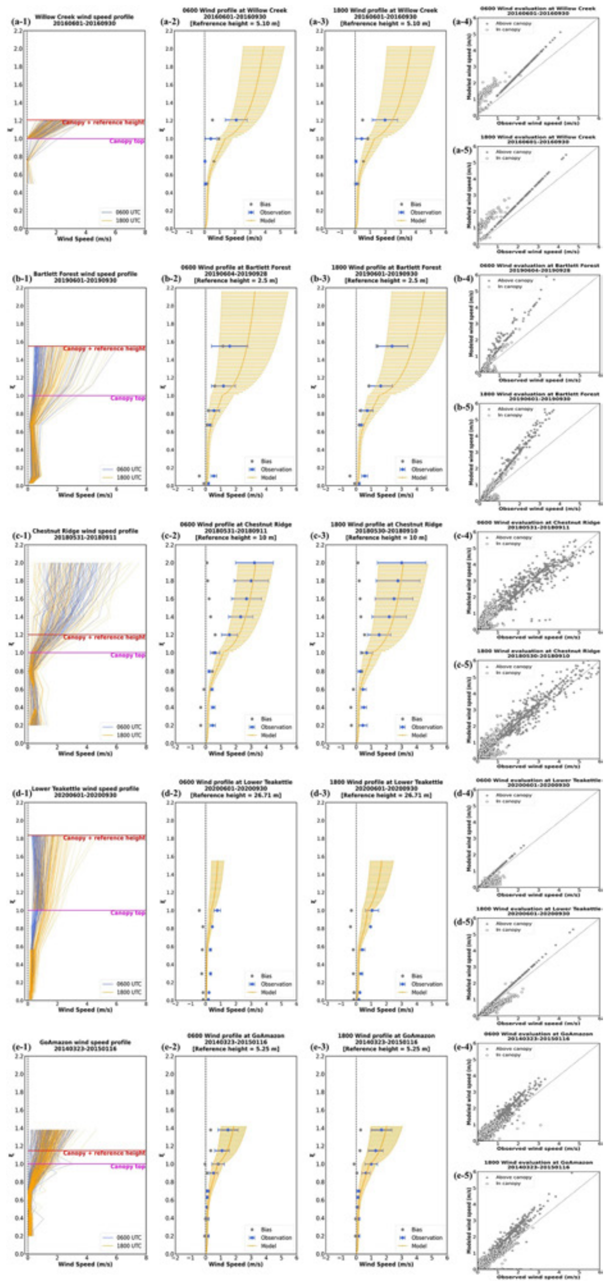

Figure 3. Observed horizontal wind profiles (far left panels), comparisons of model wind profile with observations at 0600 UTC and 1800 UTC (middle two panels), and scatter plots of observed and model wind speeds at 0600 UTC and 1800 UTC (far right panels) at (a) Willow Creek, (b) Bartlett Experimental Forest, (c) Chestnut Ridge, (d) Lower Teakettle, and (e) GoAmazon sites. In the observation plots (far left), blue and orange lines are the horizontal wind profiles at 0600 UTC and 1800 UTC, respectively. Pink and red horizontal lines show the height of the canopy top (i.e., $\xi = 1$) and the measurements at the first level above the canopy top, respectively, and the distance between the two heights is the reference height. The comparison profile plots (middle two) show the mean and range of wind speeds for model results (orange profiles) and observations (blue dots) across site-specific time periods (see Table 4), and the gray dots show the associated mean biases (model—observation). The scatter plots (far right) show the model wind speeds and observations above (filled circles) and within (non-filled circles) the canopy.

measurement height at US-xTE site (58.71 m) is beyond the maximum model level (50 m) and thus the measurements at this level are not available for evaluation. Table 6 shows the average observed wind speeds, the mean absolute biases (MABs) between model and observed mean wind profiles, and the root mean square errors (RMSEs) and coefficients of determination (R^2) of observed and model wind speeds. Mean absolute biases, RMSEs and R^2s for the in-canopy section of the full wind profiles (i.e., wind profiles within the canopy) are also calculated. Overall, the shape of model wind profiles is generally consistent with previous studies (Abolafia-Rosenzweig et al., 2021; Andrews, 2012; Bonan et al., 2018; Harman & Finnigan, 2007). Model wind profiles all show a similar pattern with a logarithmic profile above the canopy, associated with the MOST+ RSL effects, and an approximately exponential profile within the canopy that is affected by canopy density. Furthermore, a turning point at the canopy top is found in model wind profiles (Figure 3) due to the transition from the MOST + RSL effects above the canopy to foliage/drag effects below the canopy top.

The model wind profiles generally capture the variation of wind speeds with the range and average of MABs (RMSEs) around -0.25–0.56 m s^{-1} (0.13–0.70 m s^{-1}) and ~0.18 m s^{-1} (~0.40 m s^{-1}), respectively, and the average values for R^2 is around 0.90. The comparable MABs, RMSEs and R^2s for daytime and nighttime indicate that the canopy wind model captures well the diurnal variability of wind speeds. Additionally, relatively larger biases are commonly found near the canopy top ($\xi \sim 1$) for all sites (Figure 3), suggesting the influence of the MOST + RSL effects and the uncertainties of the simple RSL influence function (λ_{rs}) used in u_c estimation (Equation 10) when adjusting wind speeds from the reference height to canopy top. The use of a constant $\lambda_{rs} = 1.25$ to estimate the RSL effect above the canopy top is indeed simplified, while in reality the RSL effect is highly variable due to canopy characteristics and atmospheric stability (Abolafia-Rosenzweig et al., 2021; Bonan et al., 2018; Harman & Finnigan, 2007, 2008; Physick & Garratt, 1995). Furthermore, since in-canopy wind speeds ($u(\xi)$ are proportionally adjusted based on initial u_c values (Equation 8), the biases in u_c estimation propagate downward and impact $u(\xi)$ estimation in the canopy wind model. For instance, positive biases at the canopy top tend to result in an overestimation of in-canopy wind speeds at US-WCr site, while negative biases at the canopy top lead to a general underestimation of in-canopy wind speeds at US-xTE sites. These results emphasize the critical role of u_c estimation in in-canopy wind speed estimation and possible uncertainties from the selection of λ_{rs}.

3.2. In-Canopy Wind Profile Comparison

The previous section demonstrated the significant impacts of the MOST + RSL approximations on calculation of u_c and resulting in-canopy winds. Thus, this section focuses on evaluating only in-canopy portion of the full wind profiles. This is accomplished by constraining the upper boundary of the canopy wind model via the use of observed wind speeds near the canopy top as the reference (i.e., $h_{ref} = 0$). This approach effectively removes the uncertainties from the MOST + RSL approximation above the canopy. Results at four of the sites with wind measurements near the canopy top (US-WCr, US-Chr, US-xTE, and GOA sites) are analyzed in Figure 4 and Table 7.

Overall, model results show good agreement with observations, as the range and average of MABs (RMSEs) is around -0.18–0.06 m s^{-1} (0.12–0.33 m s^{-1}) and -0.05 m s^{-1} (0.20 m s^{-1}), respectively, and average R^2s over 0.70. There is a general underestimation of model in-canopy wind speeds compared to

Table 6
Average Observed Wind Speeds (m s^{-1}) and Mean Absolute Biases (m s^{-1}) of Average Wind Profiles, and Root Mean Square Errors (m s^{-1}) and Coefficients of Determination (R^2) of Observed and Model Wind Speeds at Selected Sites With Specific Reference Heights (i.e., $h_{ref} \neq 0$) at 0600 and 1800 UTC

	0600 UTC				1,800 UTC			
Site	Wind speed (m s^{-1})	Mean absolute bias (m s^{-1})	Root mean square error (m s^{-1})	R^2	Wind speed (m s^{-1})	Mean absolute bias (m s^{-1})	Root mean square error (m s^{-1})	R^2
Full wind profile								
US-WCr	1.04 ± 1.04	0.56 ± 0.27	0.63	0.90	1.01 ± 1.02	0.50 ± 0.26	0.56	0.90
US-xBR	0.61 ± 0.69	0.25 ± 0.51	0.56	0.94	0.95 ± 0.95	0.36 ± 0.60	0.70	0.97
US-Chr	1.49 ± 1.33	0.16 ± 0.32	0.35	0.87	1.42 ± 1.38	0.13 ± 0.30	0.33	0.91
US-xTE	0.44 ± 0.31	−0.18 ± 0.15	0.23	0.74	0.68 ± 0.65	−0.16 ± 0.18	0.24	0.93
GOA	0.53 ± 0.60	0.07 ± 0.11	0.13	0.81	0.64 ± 0.67	0.08 ± 0.14	0.16	0.80
Average	0.82 ± 0.39	0.17 ± 0.24	0.38 ± 0.19	0.85 ± 0.07	0.94 ± 0.28	0.18 ± 0.23	0.40 ± 0.20	0.90 ± 0.06
Full wind profile within the canopy ($\xi \leq 1$)								
US-WCr	0.30 ± 0.36	0.57 ± 0.32	0.88	0.66	0.31 ± 0.36	0.50 ± 0.30	0.84	0.68
US-xBR	0.34 ± 0.25	−0.06 ± 0.23	0.25	0.59	0.44 ± 0.31	−0.01 ± 0.26	0.28	0.63
US-Chr	0.44 ± 0.22	0.04 ± 0.37	0.41	0.13	0.47 ± 0.30	−0.02 ± 0.33	0.40	0.27
US-xTE	0.37 ± 0.23	−0.23 ± 0.09	0.28	0.60	0.49 ± 0.41	−0.23 ± 0.09	0.25	0.89
GOA	0.35 ± 0.39	0.02 ± 0.08	0.21	0.65	0.35 ± 0.39	0.03 ± 0.10	0.22	0.70
Average	0.36 ± 0.05	0.07 ± 0.27	0.41 ± 0.25	0.52 ± 0.20	0.41 ± 0.07	0.03 ± 0.25	0.40 ± 0.23	0.63 ± 0.20

Note. Absolute bias is calculated as model - observation. The averages across selected sites are also calculated.

observations, except for US-WCr and GOA sites with MABs close to zero. The best agreement appears at US-xTE site with the lowest MABs and RMSEs (~-0.05 and 0.12 m s^{-1}, respectively) and the highest R^2 (>0.90). The similar range of MABs across four sites indicates good representation of the foliage shape distribution function $f_a(\xi)$ for various canopy types. Moreover, model results are significantly improved compared to those affected by the MOST + RSL approximations used in the full wind profile comparisons (see Figure 3 and Table 6), with lower MABs at US-WCr and US-xTE sites, and higher values of R^2 at all sites. Note that the magnitude of MABs for in-canopy winds at US-Chr site are actually lower (Table 6: 0.04 ± 0.37 m s^{-1}) when using a reference height above the canopy (i.e., $h_{ref} = 10$ m), when compared to the in-canopy only evaluation (Table 7: -0.18 ± 0.21 m s^{-1}) using a boundary condition at the canopy top (i.e., $h_{ref} = 0$). This is due to the relatively large positive MAB near the canopy top at US-Chr (Figure 3c) that compensates for the negative MAB below the canopy, underscoring the importance of MOST + RSL approximations in deriving u_c for in-canopy wind estimation. A similar situation happens at GOA site, although the negative MAB near the canopy top (Figure 3e) that compensates for the positive MAB below the canopy, leading to relatively lower MABs (Table 6: 0.03 ± 0.10 m s^{-1}) when using a reference height above the canopy (i.e., $h_{ref} = 5.25$ m) compared to the in-canopy only (i.e., $h_{ref} = 0$) evaluation (Table 7: 0.06 ± 0.10 m s^{-1}).

Naturally, there are both mean and turbulent components of the actual winds that mix air of different wind speeds both above and within the canopy. At the flux tower sites, using eddy covariance one can artificially separate the winds (which the sonic anemometers measure fairly accurately) into its mean and turbulent components. The results suggest, however, that the relatively simple and efficient analytical canopy wind model for the attenuation of the above canopy wind speeds can well capture the profile distribution of observed, actual winds.

Moreover, in-canopy wind profiles are further separated into the upper ($\xi > 0.6$) and lower ($\xi < 0.6$) parts of the canopy to better understand the representativeness of foliage distribution shape function. The average wind speeds and MABs between the model and observed mean wind profiles, and RMSEs and R^2s of model and observed wind speeds in two categories are calculated (Table 7). The boundary of the upper and lower canopy ($\xi = 0.6$) is determined based on the height of the maximum plant density (ξ_{max}; Table 1). Results show that the average wind speeds in the upper canopy are about 2–4 times larger than those in the lower canopy, except for US-Chr site, where the average wind speeds in the upper and lower canopies are comparable. The higher wind speeds

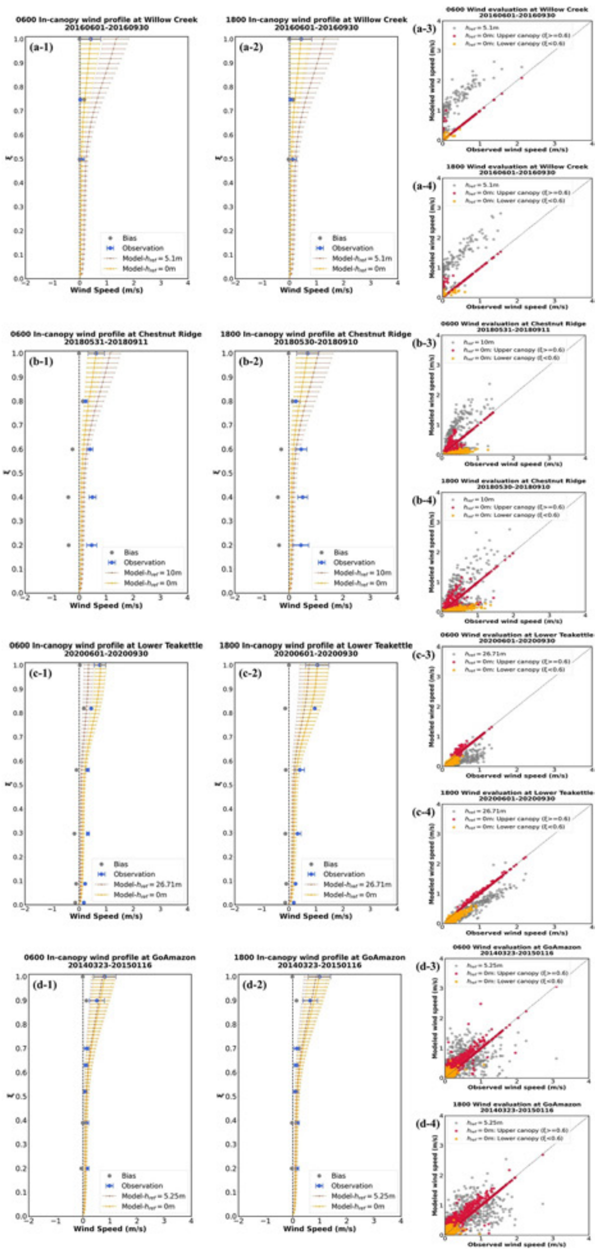

Figure 4. In-canopy wind profile at 0600 UTC (left panel) and 1800 UTC (middle panel) and scatter plots of observed and model wind speeds at 0600 UTC and 1800 UTC (right panel) at (a) Willow Creek, (b) Chestnut Ridge, (c) Lower Teakettle, and (d) GoAmazon sites. In the in-canopy wind profiles (left and middle), brown and orange profiles show the mean and range of in-canopy wind speeds for the model with $h_{ref} \neq 0$ and $h_{ref} = 0$, respectively, and blue dots show the mean and range of in-canopy wind speeds for observations. Gray dots are the mean biases between the model result with $h_{ref} = 0$ and observation (model result—observation). The mean and range are calculated for the time periods at each site (Table 4). In the scatter plots, gray dots are the paired in-canopy wind speeds of observations and model results with $h_{ref} \neq 0$, while red and orange dots are the paired in-canopy wind speeds of observations and model results with $h_{ref} = 0$ at the upper and lower canopies, respectively.

in the upper canopy are expected because wind speeds reduce with increasing distance downward from the canopy top (Massman et al., 2017). However, model biases show an opposite trend, while the average MABs and RMSEs are relatively lower in the upper canopy, and then increase in the lower canopy. The model wind speeds also show significantly better agreements with observations in the upper canopy (average $R^2 \sim 0.9$) compared to the lower canopy (average $R^2 \sim 0.1$–0.3). In addition, the canopy wind model shows larger underestimates of the wind speeds in the lower canopy at US-Chr (Figure 4b) and US-xTE (Figure 4c) compared with other sites. The larger wind speeds in observations may be impacted with the relatively minimal canopy understories at US-Chr and US-xTE sites. If there are fewer branches and leaves near the bottom of forest canopies compared to the amount of drag assumed by the canopy wind model, the observed wind speeds are less restricted and thus introduce secondary increases within the lower part of the canopy (Boudreault et al., 2014; Shaw, 1977). This phenomenon, however, could also be associated with stronger in-canopy turbulence affected by the terrain and real plant foliage (see above discussion and further information in Raupach & Thom, 1981). In other words, the foliage distribution shape function $f_a(\xi)$ used for $u(\xi)$ estimation in the canopy wind model cannot resolve the secondary increases in wind speeds (Figure 1). Furthermore, the secondary increases may also depend on canopy type, season, and other atmospheric dynamical/stability effects. The strong wind speeds exceeding 6 m s^{-1} at $\xi = 0.4$–0.6 are occasionally observed at GOA site during nighttime, indicating a potential diurnal dependence of the secondary increases (e.g., nocturnal jet effects (Bai & Schumacher, 2020)). In addition, most popular wildfire fuel data sets (e.g., LANDFIRE (https://landfire.gov/about.php)) are based on satellite measurements which often do not provide information of the canopy structure within the forest. Hence, it is difficult for the canopy wind model to simulate the secondary peaks without abundant observations and explicit foliage density profiles from regional to global scales in NWP application. Note that the nighttime gusts at GOA site are identified as outliers (i.e., strong wind speeds that are generally larger than 6 m s^{-1} and exceed the mean plus three times of standard deviation $\sim$5.8 m s^{-1}) and are omitted from the analysis.

3.3. Model Sensitivity

The sensitivity of the canopy wind model to canopy characteristics is investigated by examining three key model configurations: PAI options, vegetation type and vertical layer resolution. Three PAI estimation approaches are available in the canopy wind model, including the vegetation-type dependent PAI look-up tables from Katul et al. (2004), PAI parameterizations based on Equation 19 from M17, and retrieval from user-defined LAI based on the PAI-LAI relationship from Zou et al. (2009). User-defined, spatially-constant PAI is also available as the fourth option. PAI has a decisive impact on the canopy density profile $h_a(\xi)$ (Equation 1) and the calculation of total drag area (Equation 5). The estimations of d and z_0 are also affected as they are functions of and total drag area and canopy stress (Equation 5 and Appendix 1). Meanwhile, vegetation type determines the necessary parameters for canopy density profile estimation (Table 1 and Figure 1), the PAI value when the Katul PAI option is used, and the woody-to-total ratio (α) for PAI estimation when LAI input is provided (Equation 17). This sensitivity test focuses on the impacts of vegetation type on canopy density profile estimation and PAI values by using the PAI look-up tables from Katul et al. (2004).

Table 7
Average Observed Wind Speeds (m s^{-1}) and Mean Absolute Biases (m s^{-1}) of Average In-Canopy Wind Profiles, and Root Mean Square Errors (m s^{-1}) and Coefficients of Determination (R^2) of Observed and Model Wind Speeds at Selected Sites With $h_{ref} = 0$ at 0600 and 1800 UTC

	0600 UTC				1,800 UTC			
Site	Wind speed (m s^{-1})	Mean absolute bias (m s^{-1})	Root mean square error (m s^{-1})	R^2	Wind speed (m s^{-1})	Mean absolute bias (m s^{-1})	Root mean square error (m s^{-1})	R^2
In-canopy wind profile with $h_{ref} = 0$								
US-WCr	0.30 ± 0.36	0.05 ± 0.08	0.14	0.85	0.31 ± 0.36	0.04 ± 0.08	0.16	0.83
US-Chr	0.44 ± 0.24	−0.18 ± 0.21	0.30	0.25	0.47 ± 0.30	−0.18 ± 0.21	0.33	0.36
US-xTE	0.37 ± 0.23	−0.05 ± 0.12	0.12	0.91	0.49 ± 0.41	−0.10 ± 0.05	0.12	0.97
GOA	0.29 ± 0.33	0.01 ± 0.04	0.16	0.83	0.35 ± 0.39	0.06 ± 0.10	0.18	0.85
Average	0.35 ± 0.06	−0.04 ± 0.09	0.18 ± 0.07	0.71 ± 0.27	0.41 ± 0.08	−0.05 ± 0.10	0.20 ± 0.08	0.75 ± 0.23
In-canopy wind profile in the upper canopy ($\xi > 0.6$)								
US-WCr	0.36 ± 0.38	0.08 ± 0.09	0.15	0.85	0.37 ± 0.39	0.07 ± 0.08	0.16	0.84
US-Chr	0.43 ± 0.30	0.07 ± 0.08	0.19	0.85	0.48 ± 0.37	0.06 ± 0.07	0.23	0.88
US-xTE	0.66 ± 0.24	0.10 ± 0.08	0.07	0.94	1.02 ± 0.39	−0.07 ± 0.06	0.04	0.99
GOA	0.48 ± 0.40	0.02 ± 0.02	0.19	0.83	0.60 ± 0.45	0.09 ± 0.11	0.21	0.86
Average	0.48 ± 0.11	0.07 ± 0.03	0.15 ± 0.05	0.87 ± 0.04	0.62 ± 0.25	0.04 ± 0.06	0.16 ± 0.07	0.89 ± 0.06
In-canopy wind profile in the lower canopy ($\xi \leq 0.6$)								
US-WCr	0.07 ± 0.10	0.00	0.11	0.08	0.11 ± 0.15	−0.4	0.13	0.08
US-Chr	0.45 ± 0.15	−0.35 ± 0.05	0.42	0.05	0.47 ± 0.23	−0.35 ± 0.07	0.44	0.20
US-xTE	0.26 ± 0.08	−0.13 ± 0.03	0.14	0.41	0.29 ± 0.15	−0.12 ± 0.01	0.14	0.78
GOA	0.12 ± 0.08	−0.01 ± 0.04	0.10	0.02	0.14 ± 0.09	0.04 ± 0.08	0.11	0.00
Average	0.23 ± 0.15	−0.12 ± 0.14	0.19 ± 0.13	0.14 ± 0.16	0.25 ± 0.14	−0.21 ± 0.18	0.21 ± 0.14	0.27 ± 0.31

Note. The averages across selected sites are also calculated. Note that there is only one measurement in the lower canopy at US-WCr site.

The in-canopy wind profile at 0600 UTC with $h_{ref} = 0$ at US-xTE site (Figures 4c–4l) is used as the test case. US-xTE site is selected because of the multiple wind measurements from the surface to canopy top, the lack of significant nighttime gusts, and the good agreement between model simulations and observations at this site. The nighttime wind profile is selected to minimize the potential effect of boundary-layer turbulence due to daytime surface heating. The average LAI value at US-xTE site is about 1–3 m^2 m^{-2} according to field measurements (Tang et al., 2014), and VIIRS LAI values are similarly around 1.5–2 m^2 m^{-2}. By default, the model layer resolution is set as 0.5 m, vegetation type is set as evergreen forest, and PAI is 3.5 m^2 m^{-2}, as determined using the Katul et al. (2004) look-up table. The model sensitivity to a specific parameter is evaluated by modifying the parameter of interest while keeping others unchanged.

Results of in-canopy wind profiles using different model configurations are shown in Figure 5 and Table 8. Overall, the canopy wind model shows a high sensitivity to PAI options (Figures 5a and 5b). For user-defined PAI (Figure 5a), PAI values on the low (high) end of what is observed at US-xTE site (∼1–3 m^2 m^{-2}) leads to weaker (stronger) drag effect and wind reduction, and results in over (under) predictions of in-canopy wind speeds (Figure 5a). From this sensitivity test, it appears that a PAI value of 2 m^2 m^{-2} generally provides the best agreement for model in-canopy winds compared to observations with the lowest MAB and RMSE (Table 8), indicating that a PAI value of 2 m^2 m^{-2} is representative of the canopy characteristics at this site.

As for the PAI estimation approaches (Figure 5b), the PAI values based on the look-up table from Katul et al. (2004), Equation 19 from M17 and VIIRS LAI are 2.90, 15.81 and 1.77 m^2 m^{-2}, respectively. The variability of the shape of in-canopy wind profile reflects the diversity of PAI values among three approaches as the highest PAI based on the Equation 19 from M17 results in the strongest wind reduction effects. The PAI look-up tables from Katul et al. (2004) generally provide a better estimation of PAI values and good agreement with measured mean in-canopy wind speed profiles. The PAI parameterization from M17 generates overestimated PAI

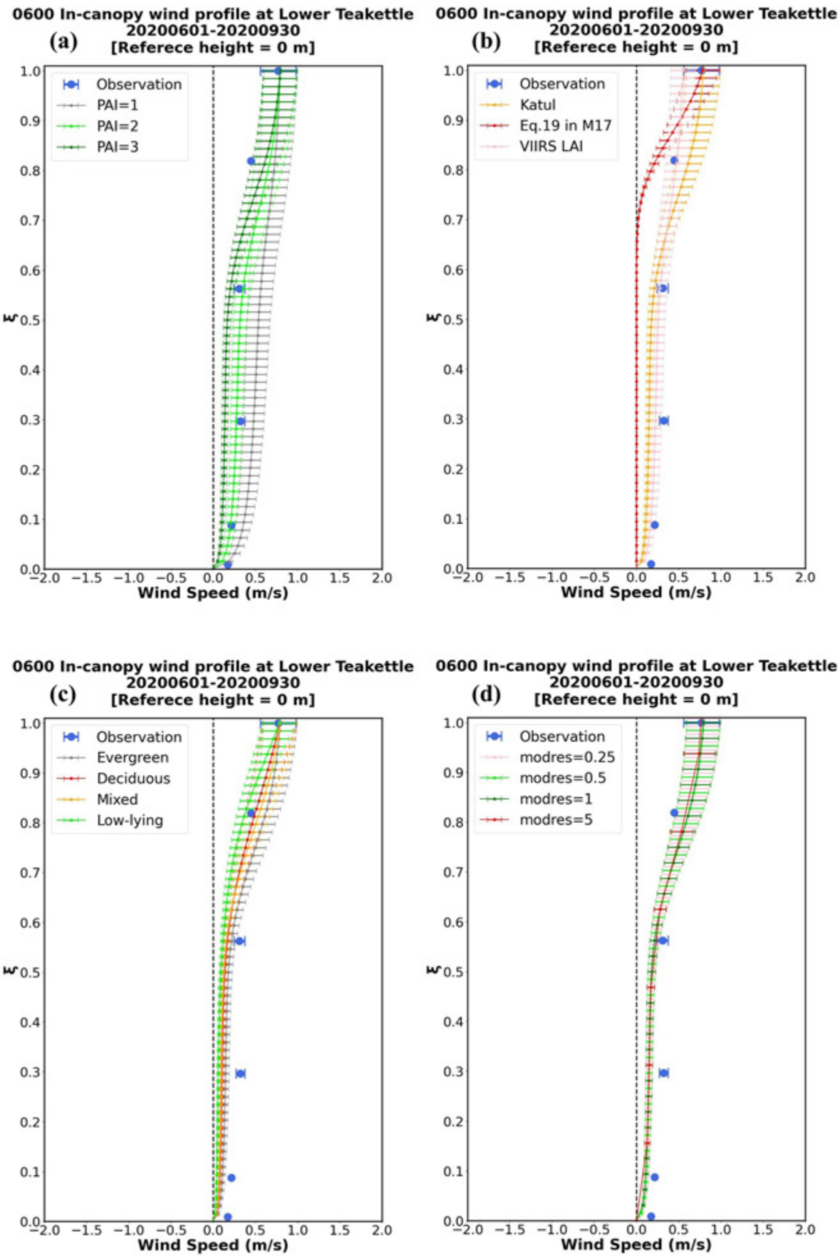

Figure 5. In-canopy wind profiles with (a) user-defined plant area index (PAI) values of 1–3, (b) PAI estimation based on the Katul et al. (2004) look-up table, Equation 19 in M17 and VIIRS LAI retrieval, (c) four vegetation categories, and (d) vertical layer resolution of 0.25, 0.5, 1 and 5 m at Lower Teakettle site, 0600 UTC. The model configuration for each run is the same except for the listed parameters.

values and underestimated in-canopy wind speeds (Figure 5b). The PAI overestimation of the Equation 19 in M17 is influenced by its dependence on canopy height and canopy fraction, which leads to high PAI in dense and tall forests (i.e., large values of canopy height and canopy fraction). Also, the experiment using LAI-derived PAI demonstrates the reliability of VIIRS LAI retrievals and the PAI-LAI relationship, and further supports previous studies (Xiao et al., 2016; Xu et al., 2018; Yan et al., 2018) from a perspective of in-canopy wind estimation.

The canopy wind model also shows a high sensitivity to canopy type (Figure 5c), mainly associated with its contribution to the estimation of PAI and canopy density shape. The PAI values for evergreen forest, deciduous forest, mixed forest, and low-lying vegetation are 2.90, 4.10, 3.71 and 3.02 $m^2\ m^{-3}$, respectively, showing a small variability compared with those derived from different PAI estimation approaches. The model results mainly

Table 8
Mean Absolute Biases (m s^{-1}) and Root Mean Square Errors (m s^{-1}) of Model In-Canopy Wind Profiles With h_{ref} = 0 Compared to Observations at US-xTE Site, 0600 UTC

Model configuration	Mean absolute bias (m s^{-1})	Root mean square error (m s^{-1})
PAI option		
User-defined PAI = 1	0.13 ± 0.12	0.19
User-defined PAI = 2	0.02 ± 0.10	0.09
User-defined PAI = 3	−0.05 ± 0.12	0.13
PAI option = Katul	−0.05 ± 0.12	0.12
PAI option = Equation 19 in M17	−0.20 ± 0.11	0.24
PAI derived from VIIRS LAI	−0.08 ± 0.08	0.14
Vegetation type		
Evergreen forest	−0.05 ± 0.12	0.12
Deciduous forest	−0.10 ± 0.10	0.14
Mixed forest	−0.09 ± 0.11	0.15
Low-lying vegetation	−0.14 ± 0.09	0.18
Model layer resolution		
5 m	−0.07 ± 0.11	0.12
1 m	−0.06 ± 0.12	0.12
0.5 m	−0.05 ± 0.12	0.13
0.25 m	−0.05 ± 0.12	0.13

Note. The model configuration for each run is the same except for the listed parameters.

diverge in the upper canopy, above $\xi \sim 0.6$, due to varying canopy density functions for four canopy types (Figure 1). Overall, the influence of vegetation type on the in-canopy wind calculation in terms of the determination of PAI values and drag coefficients based on the look-up table from Katul et al. (2004) is minor.

The canopy wind model generates comparable results with different vertical layer resolution, showing negligible sensitivity to model layer resolution (Figure 5d). The differences of MAB and RMSE are minor even when the model layer resolution is increased by 20-fold (5 m compared to 0.25 m) (Table 8). This finding indicates that the canopy wind model provides reliable results when run at coarser vertical resolutions, thereby making the canopy wind model computationally efficient and thus beneficial to regional and global NWP applications.

4. Application to Regional NWP Modeling

As an extension of the single-point approach in M17, the canopy wind model is able to provide the estimation of the three-dimensional structure of horizontal wind speeds and canopy effects by using two-dimensional gridded data sets over any given domain as inputs. To estimate the influence of the canopy on wind speeds, the canopy wind model first identifies and defines the lower thresholds for presence of vegetation. For instance, model grids with a user-defined canopy height >0.5 m, canopy fraction >0.1, and LAI >0.1 m^2 m^{-2} are used as filters to identify canopy grids, whereas elsewhere the grid cells are ignored in the model simulation. It should be noted that these are relatively low thresholds for the presence of contiguous forest canopies; however, this work aims to demonstrate the influence of the canopy wind model across a range of vegetation heights above the surface. Ultimately, such model grid cells are still only considered if there is a valid climatological forest height observed by the gridded satellite product, hence suggesting the presence of a forest canopy.

In this section, model results using two-dimensional gridded data sets over the CONUS are discussed. The example of gridded model results shown here uses the model configurations including model maximum height as 50 m, model layer resolution as 0.5 m, reference height as 10 m, PAI values based on the look-up table from Katul et al. (2004), and the canopy filters listed previously. The following discussion primarily focuses on forest

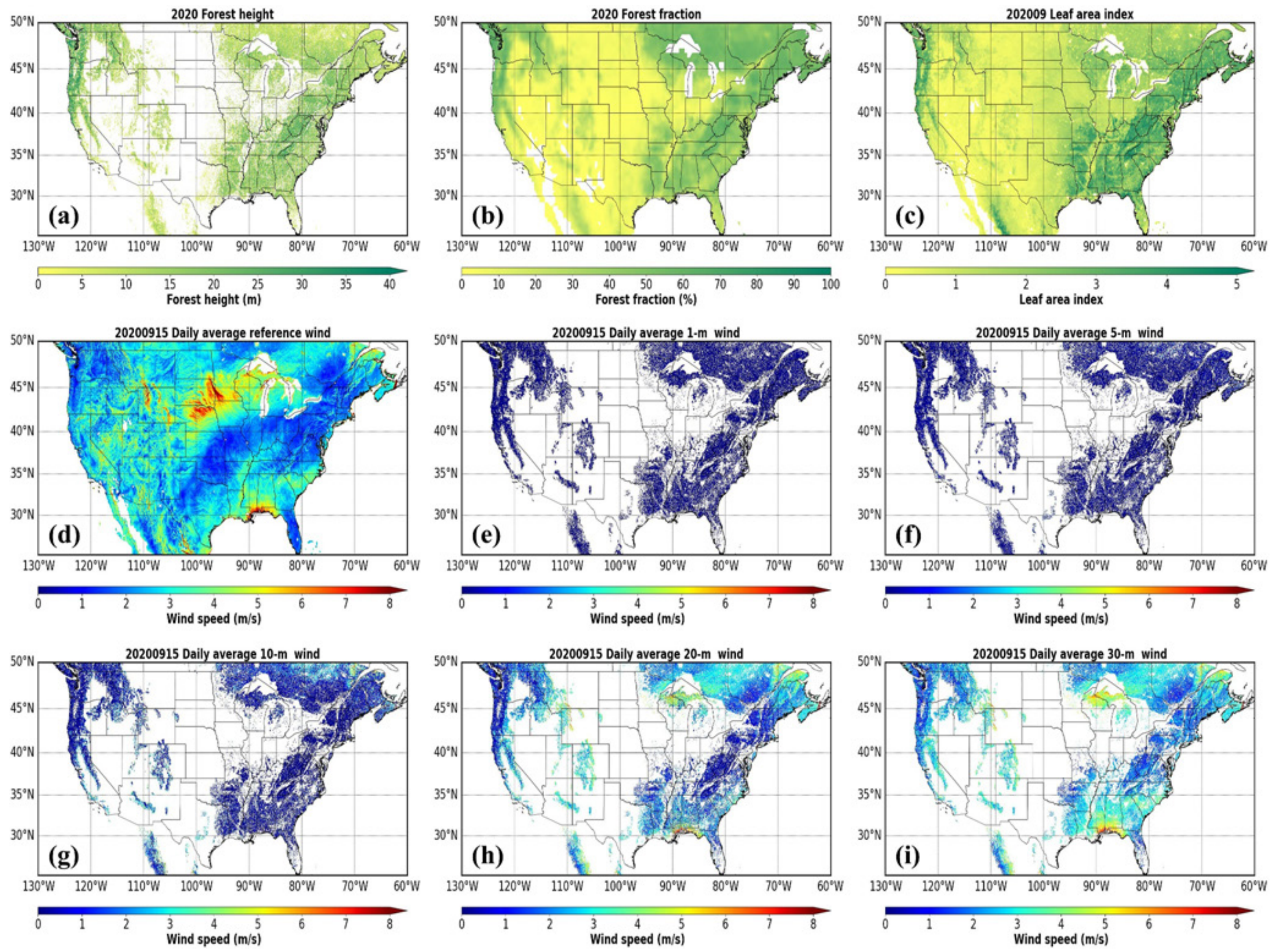

Figure 6. The (a) global ecosystem dynamics investigation climatological forest height in 2020, (b) MODIS climatological forest fraction in 2020, (c) monthly average of VIIRS LAI in September 2020, and (d) daily average of horizontal wind speed at 10 m above the canopy (where present) from HRRRv3 (reference wind) on 15 September 2020. The daily average of horizontal wind speeds at (e) 1, (f) 5, (g) 10, (h) 20, and (i) 30 m above the ground affected by canopies on 15 September 2020. (a–d) are used as inputs to the canopy wind model, and (e–i) are model results. Note that the regions identified as without a canopy are ignored in the canopy wind model.

regions, as it is these regions with the most significant data availability, contiguous canopy coverage, and overall in-canopy wind reduction. Therefore, forest height and forest fraction are used as the proxy of canopy height and canopy fraction, respectively, in the following discussions. Note that all the model results shown in this section are based on the same model configurations, except for the WAF assessment in Section 4.3 in which a 2020 Californian fire case is discussed.

4.1. Spatially Varying Horizontal Wind Speeds and Canopy Effects

Figures 6a–6c illustrates the gridded canopy height, canopy fraction, and LAI over the CONUS from September 2020 (same for March 2020 in Appendix Figure B1). The example reference wind speed is based on the horizontal wind speeds at 10 m above the surface from the HRRRv3 initial analysis field (Figure 6d). Like most NWP models, HRRRv3 relies on the "big-leaf" approach and a MOST surface-layer parameterization, where the surface is treated as bare soil and/or vegetation with no explicit vertical representation (Dowell et al., 2022). Thus, the HRRRv3 diagnostic 10-m wind is technically taken 10 m above the canopy (where present), and derived from the entire model prognostic log wind profile that goes to zero at the height of the surface element's roughness length plus the displacement height (dependent on prescribed vegetation type). Therefore, the height of the HRRRv3 diagnostic 10-m wind above ground is not exactly 10 m and varies by spatially dependent canopy height.

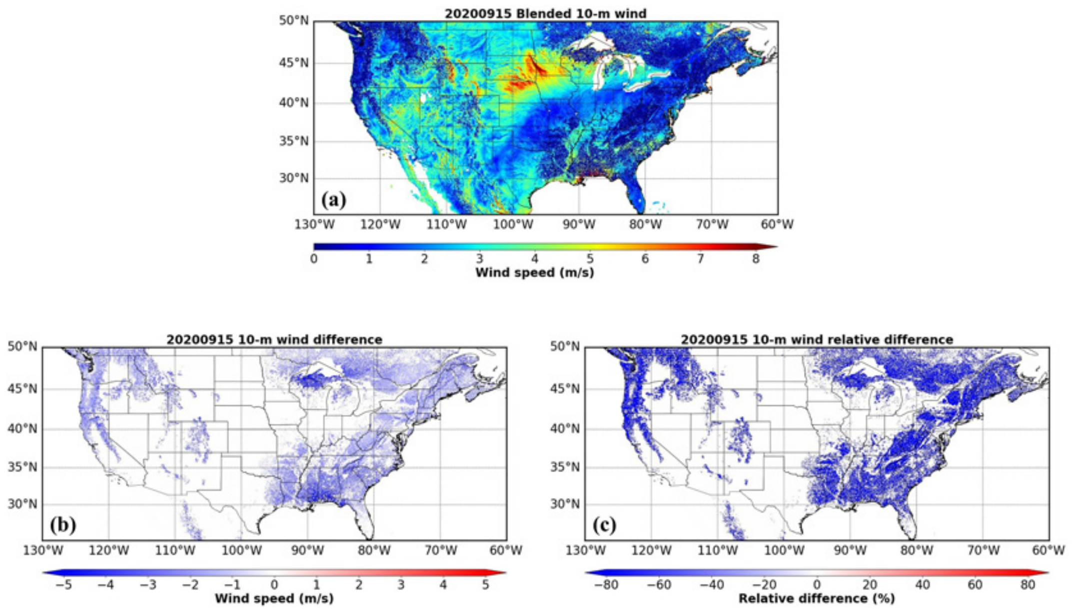

Figure 7. (a) Blended daily average of 10-m wind speeds on 15 September 2020, and (b) absolute difference and (c) relative difference between the 10-m wind speeds obtained by the canopy wind model and 10-m reference wind speeds (i.e., model–reference).

Figures 6e–6i shows the horizontal wind speeds at various levels from 1 to 30 m above the ground considering the influence of canopy, with inclusion of the full wind profile (i.e., from the surface to model maximum height 50 m for above and below the canopy top) generated by the canopy wind model. Grid cells that do not satisfy the canopy filters (canopy height > 0.5 m, canopy fraction > 0.1, and LAI > 0.1 m^2 m^{-2}) are transparent. Most forests are taller than 5 m (Figure 6a ~97%), and thus the 1-m and 5-m wind speeds (Figures 6e and 6f) have widespread reductions compared with the reference wind speeds (Figure 6d). Due to the influence of an explicitly defined canopy wind model here, the calculated 10-m wind speeds above the ground are less than 2 m s^{-1} over ~75% of all forests (Figure 6g). Moreover, wind speeds increase when heights become higher within or above the canopy top. For instance, 30-m wind speeds are about double that of 20-m wind speeds over the southeastern US (Figures 6h and 6i), as the average height of the forests over this region is about 20–25 m. Thus, the 30-m wind speeds are generally above the forest canopy tops in this region. However, 30-m wind speeds are significantly reduced in the western US, where about 20% of identified forests are taller than 30 m.

Figure 7a is an example of the blend of simulated 10-m wind speeds at identified forest grids and reference wind speeds (i.e., HRRRv3 diagnostic 10-m wind speeds) at canopy-free grids that do not satisfy the canopy filters (canopy height < 0.5 m, canopy fraction < 0.1, and LAI < 0.1 m^2 m^{-2}). By assuming canopy height equals to 0 m at canopy-free grids, reference wind speeds at those grids could be used as the approximations of actual 10-m wind speeds above the ground. Figures 7b and 7c show the absolute difference and relative difference between the wind speeds simulated by the canopy wind model and reference wind speeds (difference = model—reference). The blended wind speeds may be more representative of the near-surface airflow, as the reference wind speeds, technically, are the diagnostic wind speeds at 10 m above the canopy instead of 10 m above the ground. In practice, the typical 10-m wind speeds from NWP models can serve as a first guess for in-canopy wind speed estimation to generate the blended wind speeds. It is important to mention that canopy fraction of 0.1 and LAI of 0.1 m^2 m^{-2} suggest a sparse vegetative canopy, which may introduce uncertainties in the representation of in-canopy wind speed when a coarse grid resolution is used.

However, it is worth noting that the different surface parameterizations in the canopy wind model and HRRRv3 (i.e., vertically resolved canopy and "big-leaf" approach, respectively) could lead to inconsistencies in the calculations of z_0, d, and wind speeds. The inconsistencies, as a limitation of the canopy wind model, may introduce uncertainties to the blended wind speeds and future potential applications.

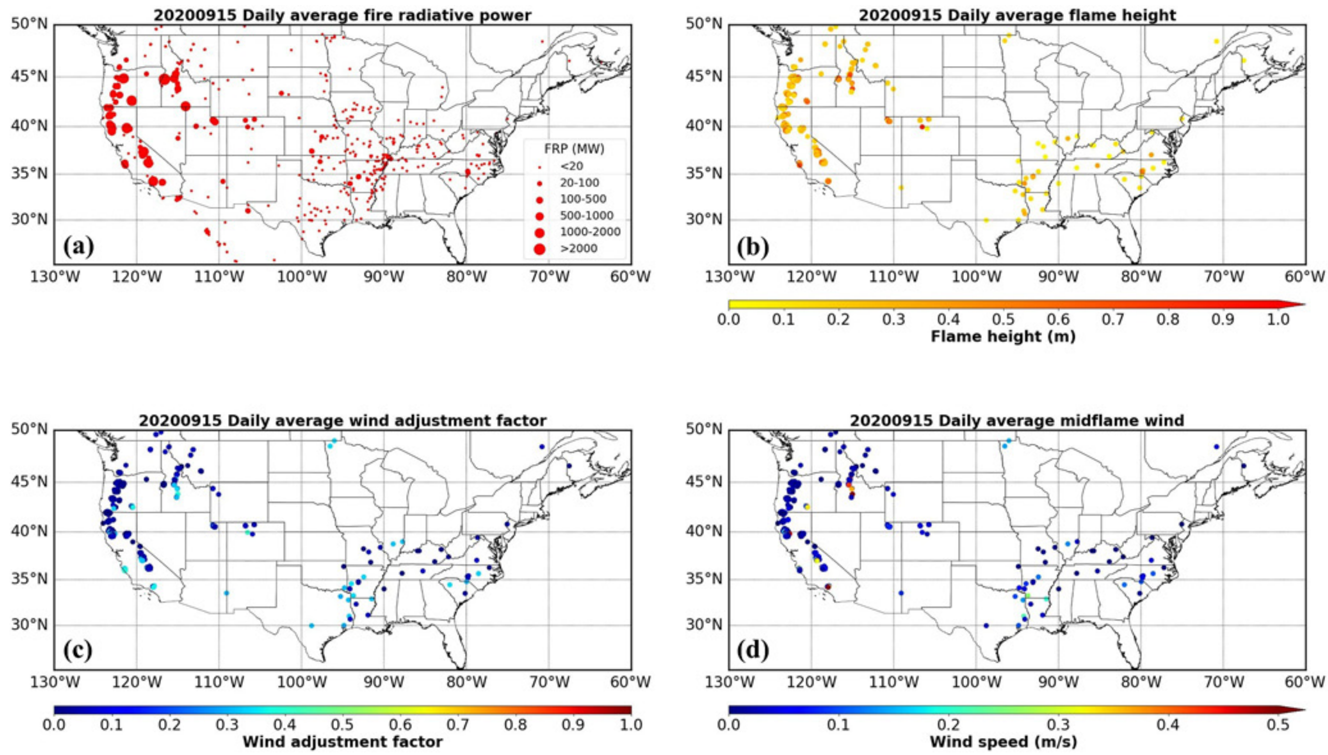

Figure 8. The daily average of (a) fire radiative power from RAVE, (b) flame height, (c) wind adjustment factor, and (d) midflame wind speeds on 15 September 2020.

4.2. Estimation of WAF and the Midflame Wind Speed

A useful application of the WAF model is the estimation of midflame wind speed (u_{mid}) of wildfires using WAF based on the results from the canopy wind model and approximated fire characteristics, thus providing valuable information for potential usage in prognostic fire spread calculations in NWP models. Verification of the WAF calculation also follows the approach in M17 and is further discussed in Appendix 3. Here the location and intensity of active wildfires are identified using the FRP product from RAVE. Daily average FRP over CONUS on 15 September 2020 is used in this study (Figure 8a).

Figure 8b illustrates the estimated midflame height (h_{flame}) following the approach described in Section 2.3. Figures 8c and 8d are the WAF and midflame wind speeds at model grids with valid canopies (i.e., passing the three canopy filters discussed previously), respectively. The wildfires in California and Oregon generally have higher flame heights about 0.3–0.5 m compared to the fires in the southeastern US due to stronger FRP exceeding 100 MW. However, wildfires in the western US show lower WAF with an average of 0.06 ± 0.11, while the average WAF over the southeastern US is about double (0.13 ± 0.14). This is because of the taller forests in the western US compared to the southeastern US. In this approach, the estimated flame heights are generally lower than 0.5 m, and thus wind speeds could be reduced significantly when occurring below the relatively tall western canopies, resulting in low WAF and midflame wind speeds. Note that the wind speeds at grids without valid canopies are assumed to be unaffected by the canopy. The midflame wind speeds for those grids should be the same as the reference wind speeds and are not discussed in this study.

4.3. Assessment of the WAF for NWP Applications

Typically, gridded fire intensity (e.g., FRP) is a known piece of information at any given forecast time in prognostic fire behavior models coupled in NWP models (e.g., WRF-FIRE (Coen et al., 2013)). With the meteorology and fire intensity provided by NWP models as well as vegetation type and external canopy data, the WAF model can calculate WAF and midflame wind speeds, which can be applied to prognostic fire behavior models for fire spread prediction and the estimation of the fire intensity for future time steps. This process can be repeated until the end of a forecast simulation.

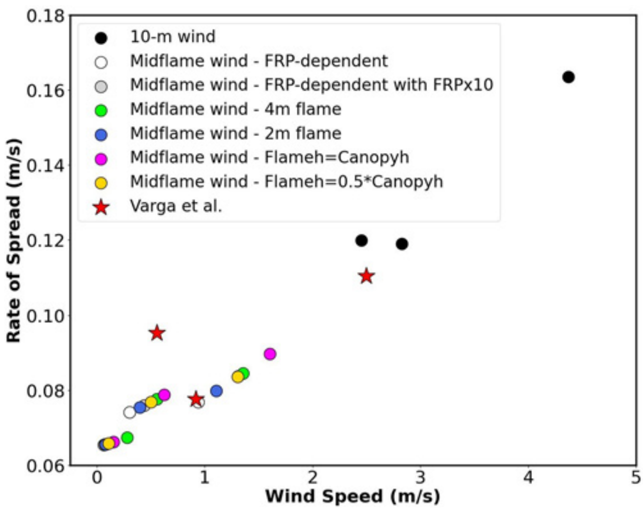

Figure 9. Comparison of the rates of spread (ROS) during the Doe Fire during 19–21 August, 2020. Colorful dots represent the ROS calculated by Rothermel's fire spread model using midflame wind speeds estimated by the wind adjustment factor (WAF) with different flame height options in the WAF model. Red stars are the ROS reported in Varga et al. (2022), in which the Canadian Forest Fire Behavior Prediction System and effective wind speeds were used. Note that the units of wind speeds and ROS from Varga et al. (2022) are converted to m s^{-1} for easy comparison.

To better understand the performance of WAF for NWP application, the midflame wind speeds estimated by the WAF from the WAF model are used to calculate the rate of spread (ROS) based on the Rothermel's surface fire spread model (Andrews, 2018; Rothermel, 1972). ROS is the propagation speed of the frontline or head of the fire and is commonly used to describe the movement of wildfires in fire behavior models. In this study, the Californian Doe Fire during 18–22 August, 2020 is selected as a case study, and the results are compared with Varga et al. (2022) that applied the Canadian Forest Fire Behavior Prediction System (CFFBPS; Forestry Canada Fire Danger Group, 1992) and evaluated its ROS estimation. The CFFBPS simulated fire perimeter agreed well with observations. In CFFBPS, ROS is driven by "net effective winds" that are adjusted based on terrain slope. Details of the Rothermel's fire spread model and CFFBPS can be found in the cited references, and a brief verification of them is shown in Appendix 4. Here, the ROS model using inputs from Varga et al. (2022) serves as an approximate method to assess and evaluate the WAF model's WAF impact. Since the fuel categorization, fuel parameters, and parameterizations of the effects of wind speeds and terrain slope on ROS are different in two models (the Rothermel's model and CFFBPS), the uncertainties associated with fuel categorizations and wind/slope effects are not discussed in this study and are beyond the scope of this work. The configurations of the WAF model results discussed in this section are the same as those used for the canopy wind model in Section 4.2, except for the time and domain of interest which are based on Varga et al. (2022), and flame height options.

Figure 9 illustrates the daily ROSs from Varga et al. (2022) and those calculated based on the WAF and midflame wind speed using different flame height options, including default FRP-dependent flame heights (ensemble approach based on Alexander and Cruz (2012)), FRP-dependent flame heights but with enhanced FRP values by applying a factor of 10, constant flame heights of 2 and 4 m, and flame heights equal to full and half that of the canopy heights. Table 9 summarizes the average wind speed, flame height and ROS for each option. Although Varga et al. (2022) reported four daily ROS values (Table 3 in Varga et al., 2022) from 18–22 August, 2020, in this case, model grids may exist that have valid FRP values but no valid canopies on 18 August in the WAF model. Such points are removed from the analysis due to the inability of the WAF model to calculate valid WAF estimates.

Results reveal that the ROSs based on midflame wind speeds show an overall comparable range with Varga et al. (2022), while 10-m wind speeds produce significantly higher ROS. This finding verifies the validity of the

Table 9
Average Wind Speeds, Flame Heights and Rates of Spread of the Doe Fire During 19–22 August From Varga et al. (2022) and Those Estimated by the Rothermel's Fire Spread Model Using Wind Adjustment Factor and Midflame Wind Speed With Different Flame Options

	Wind speed (m s^{-1})	Flame height (m)	ROS (m s^{-1})
Varga et al.	1.42 ± 0.78	-	0.090 ± 0.014
10-m wind	3.22 ± 0.83	-	0.134 ± 0.021
Midflame wind: FRP-dependent	0.44 ± 0.37	0.89 ± 0.54	0.072 ± 0.005
Midflame wind: FRP-dependent with FRPx10	0.61 ± 0.52	2.58 ± 1.55	0.075 ± 0.007
Midflame wind: 4 m flame	0.73 ± 0.46	4.00	0.077 ± 0.007
Midflame wind: 2 m flame	0.53 ± 0.43	2.00	0.074 ± 0.006
Midflame wind: $h_{flame} = h$	0.80 ± 0.60	12.81 ± 8.36	0.078 ± 0.010
Midflame wind: h_{flame} = 1/2 hr	0.64 ± 0.50	6.40 ± 4.18	0.075 ± 0.007

Note. Values for August 18th are removed from the analysis due to the lack of identified valid canopies in the WAF model. Here, h_{flame} refers to the flame height and *h* refers to the canopy height.

WAF from the WAF model, as usage of typical NWP 10-m wind speeds (i.e., wind speeds at 10 m above the canopy) are much higher than the effective wind speeds from Varga et al. (2022) and do not account for the canopy-induced wind reductions. Among all flame height options, the default FRP-dependent option shows the lowest average flame height of 1 m, leading to the lowest average midflame wind speed (0.44 ± 0.37 m s^{-1}) and ROS (0.072 ± 0.005 m s^{-1}). According to Alexander and Cruz (2012), which summarized the range of flame heights from 18 field and laboratory studies, the value of flame height varies from 0.1 m to over 10 m with an average around 2 m, while the estimated flame heights from the WAF model demonstrate a realistic range from near 0–2 m. However, gridded FRP products usually provide average FRP values per grid cell instead of values for individual fires, and likely underestimate the fire intensity after averaging. The underestimation of FRP could lead to underestimations of flame height and midflame wind speed, and eventually, an underestimation of ROS.

Further, results show the sensitivity of ROS on flame height and midflame wind speed. A positive correlation is found among the three parameters, with higher flame heights leading to stronger midflame wind speeds and ROSs. These results are consistent with the core assumptions of the WAF model and Rothermel's fire spread model, as midflame wind speeds are determined by the heights of fire midpoint, and ROSs are linearly correlated with wind speeds. Such positive correlation provides the possibility of improving ROS estimates by providing a better estimation of midflame wind speeds from the WAF model.

5. Discussion

As discussed in Section 3.3, the canopy wind model is sensitive to the selection of PAI and the overall canopy density profile that is based on a prescribed foliage distribution shape function $f_a(\xi)$. Although the vegetation-type-dependent PAI look-up table from Katul et al. (2004) introduces generally realistic results, the simplification of canopy characteristics may not properly describe realistic canopy structures, leading to possible uncertainties in the calculation of in-canopy wind profile. On the other hand, the PAI parameterization based on Equation 19 from M17 provides an "effective PAI" that considers canopy characteristics such as forest canopy height and cover fraction, as well as leaf sheltering effects (Massman et al., 2017). Further, the reclassification of canopy types (i.e., using four canopy categories rather than eight canopy types) based on M17 in this study (from eight canopy types to four categories) and the use of canopy-type-dependent prescribed foliage distribution shape function $f_a(\xi)$ may miss the regional variations of canopy density (e.g., canopy understories) for a given canopy type.

To rectify some of the uncertainties discussed above, additional canopy cover and vertical profile metrics data are available via the space-borne lidar measurements from the Global Ecosystem Dynamics Investigation (GEDI; Dubayah et al., 2021), including the vertical profiles of PAI and plant area volume density (PAVD). Several researchers have demonstrated that GEDI canopy products show generally reliable performance when compared with airborne laser measurements in temperate forests (Dhargay et al., 2022; Wang, Jia, et al., 2023, Wang, Jia, et al., 2023). Although validations on other canopy types and regions are necessary, GEDI PAI and PAVD profiles have been shown to capture realistic canopy vertical structures. Therefore, GEDI PAI and PAVD profiles could potentially improve the accuracy of in-canopy wind speed estimation by providing a better representation of the canopy density profile in the canopy wind model.

The use of a simplified RSL influence function λ_{rs} is another source of uncertainty in the in-canopy wind profile estimation, as the RSL effect varies with canopy characteristics and boundary layer conditions. Although λ_{rs} is tunable, its impacts on canopy wind profile estimation are minor and the canopy wind model nearly shows no sensitivity to the selection of λ_{rs}, probably due to the relatively limited value range in its application (Appendix 5). Harman and Finnigan (2007, 2008) proposed a more complicated and comprehensive unified RSL turbulence theory based on MOST, providing a self-consistent set of formulations of wind speeds, surface radiation and turbulent fluxes, and the surface exchange processes of heat and moisture above and within the vegetative canopies. This theory has been applied and validated in land surface models (e.g., Abolafia-Rosenzweig et al., 2021; Bonan et al., 2018; Shapkalijevski et al., 2016, 2017), showing good agreements for above- and in-canopy wind speeds. Application of such explicit RSL parameterization could potentially improve the performance of modeled in-canopy wind speeds by providing a better estimation of the wind speed and more seamlessly transitioning between regimes at the air-canopy interface.

A major concern of the WAF and midflame wind speed estimations comes from the estimation of flame height. The influence of underestimated gridded FRP on flame height and WAF estimation has been tested and discussed in Section 4.3. Also, previous studies show that most intense fires are crown fires (i.e., fires burning at the crown top), and the flame heights of these crown fires are comparable to the canopy heights (Andrews et al., 2011; Stocks et al., 2004; Taylor et al., 2004; Wagner, 1977). Fire spotting (i.e., the scatter of burned objects that could ignite new fires at distance away from the flame) is often observed in crown fires, and spotting distance is affected by wind speeds (Albini et al., 2012; Alexander & Cruz, 2011; Koo et al., 2010). Hence, the flame height derived in the WAF model might be too low, and the resultant midflame wind speeds could underestimate the speed at which crown fires spread. To address this issue, the WAF model has the flexibility to use either a constant user-defined flame height, flame heights as a fraction ($\leq$1) of canopy heights, or adjusted flame heights for crown fires. When the crown fire option is used, wildfires with fire intensity (Equation 13) greater than 1700 MW m^{-1} (Andrews et al., 2011) are identified as crown fires, and the wind speed at the canopy top (u_c) is used as the midflame wind speed. An evaluation of model simulations using different flame height options is conducted and the details are presented in Appendix 6. Results show that the influence of different flame height options may be limited over tall forest regions because the midflame point is still well within the deep canopy and the wind speeds are significantly affected by the canopy.

Moreover, fire behaviors are not explicitly simulated in the WAF model. For instance, the calculation of WAF only considers the wind reduction due to the canopy and does not account for fire behaviors and their feedback. The interaction between fires and winds is a two-way process in nature. Wind speed and direction could affect the geometrical features and spread of fires (Cheney et al., 1993, 1998; Cheney & Gould, 1995; Linn & Cunningham, 2005; Sutherland et al., 2023), while the overall dynamical circulations and resulting wind speeds near and/or within fire flames may be enhanced due to the heat released by fires (Eftekharian et al., 2018, 2019a, 2019b, 2021). Such fire feedbacks could be approximately addressed by applying an influence factor of 1–2 to the estimated midflame wind speeds according to Eftekharian et al.'s research. However, fire feedbacks are highly variable and case dependent, and are cutting-edge areas of research for canopy and/or regional to global-scale NWP models used to simulate the complexity of fire behaviors. Ultimately, bridging the gap between such local-scale fire behavior and their feedbacks and regional to global-scale NWP modeling is a major challenge facing the community today.

The canopy model set (i.e., the canopy wind model and the WAF model) currently runs as an offline standalone application with preprocessed vegetative canopy inputs. In the future, the canopy model set presented here is anticipated to be coupled with NWP models as an online canopy component via its own column physics routines (e.g., Common Community Physics Package (CCPP); https://dtcenter.org/community-code/common-community-physics-package-ccpp) or as a separate Earth System Model Framework component (e.g., NOAA's Unified Forecast System (UFS); https://ufscommunity.org/). This is envisioned by coupling and driving the canopy model set using other physical components and above canopy initializations from the land surface and planetary boundary layer models, while being supplemented by external satellite-derived vegetative canopy inputs. For instance, non-observed land surface properties (e.g., model resolved surface roughness length and friction velocity) from the land surface model, 10-m wind speeds from the weather model, and fire characteristics (e.g., FRP) from the fire behavior model components in NOAA's UFS could be used as initialized/boundary inputs for the canopy wind and WAF models, whose products (e.g., WAF and midflame wind speed) could be further passed back to the UFS weather and fire behavior models for the estimation of the spread of fire and fire forecast. This is one of the many potential applications of a future online-coupling of the canopy model within NOAA's UFS for NWP applications.

6. Conclusions

This study develops and evaluates a stand-alone, modular one-dimensional canopy model set, including a canopy wind model and a WAF model, for cross-scale NWP modeling applications. The canopy wind model is based on Massman et al. (2017), which is desirable because of its simplicity and flexibility of the asymmetric gaussian distribution function that can be applied as prescribed, vertically resolved foliage shapes for different gridded vegetation types globally. The canopy wind model provides estimations of the vertically resolved horizontal wind speeds uniformly above and below the canopy based on the MOST and simple RSL effects.

10.1029/2024MS004300

Overall, the canopy wind model well simulates the three-dimensional structure of horizontal wind speeds affected by the canopy with relatively low biases compared to vertical wind profile measurements at four Ameriflux and one GoAmazon sites. Derivation of blended canopy-resolved wind fields could provide a better representation of near-surface wind flow in regional to global NWP applications, particularly for areas covered by dense canopies. Furthermore, the WAF model is capable of estimating the wind speeds at the midflame point of active wildfires (midflame wind speed) based on fire characteristics (e.g., fire intensity), which could be used for the estimation of the rate of fire spread in fire behavior models and better represent the wind flows associated with fire behaviors.

The major sources of uncertainties in the canopy model set include (a) the use of the arbitrary shape and prescribed canopy foliage density functions applied to different vegetation types, (b) the simplified RSL influence function, (b) the biases in flame height estimation due to underestimated fire intensity and varying fuel and fire types such as crown fires, and (d) the lack of local-scale fire feedbacks on dynamical circulations and wind enhancements. Despite these potential limitations, the user-definable (and tunable) options in the canopy wind and WAF models provide users the flexibility to adjust control factors according to user applications. Also, such flexibility of adjusting FRP value and flame height provides the WAF model the potential to be integrated with fire behavior models to generate an interconnected workflow for the estimation of fire spread in NWP modeling systems. Future work includes a built-in ROS calculation based on Rothermel's fire spread model, improved 2D and 3D canopy representation using GEDI observations from space, and direct connection of the impacts of in-canopy wind and WAF model explained here to NWP and related fire behavior models, as well as improved verification against observed events within these contexts.

Appendix A: Definitions of Zero-Plane Displacement Height and Surface Roughness Length

Following Massman et al. (2017) (M17), the zero-plane displacement height (d) is calculated based on its relationship with the canopy height (h):

$$\frac{d}{h} = [1 - FRAC_*(0)] \times \frac{\int_0^1 FRAC_*(\xi)\xi d\xi}{\int_0^1 FRAC_*(\xi)\, d\xi} \tag{A1}$$

where $\xi = \frac{z}{h}$ and $FRAC_*$ is the fraction of the friction velocity at the desire height (z) to the friction velocity at the canopy top (h):

$$FRAC_*(\xi) = \frac{cosh\left[q_* N \times FRAC_d(\xi)\right]}{cosh\left(q_* N\right)}, \qquad 0 \le \xi \le 1 \tag{A2}$$

with

$$q_* = q_a + q_b\, exp\left(-q_c N\right) \tag{A3}$$

where $q_a = 4.02 - q_b$, $q_b = 2/\left(1 - e^{-1}\right)$, and $q_c = 0.6$. Note that $FRAC_d(\xi)$ is equal to $FRAC(\xi)$ as the drag effect is assumed to be independent from the winds and is dominated by canopy density in this study.

The surface roughness length (z_0) is calculated as:

$$\frac{z_0}{h} = \lambda_{rs}\left(1 - \frac{d}{h}\right) \times exp\left(-k\sqrt{\frac{2}{CTRESS}}\right) \tag{A4}$$

where $\lambda_{rs} = 1.25$ is the default value of RSL effect in the M17 model, $k = 0.4$ is the von Karman constant, and $CTRESS$ is canopy stress. Note that z_0 from the input list is used as a first guess for u_c estimation, which is further applied to $CTRESS$ and z_0/h calculation in the canopy wind model.

10.1029/2024MS004300

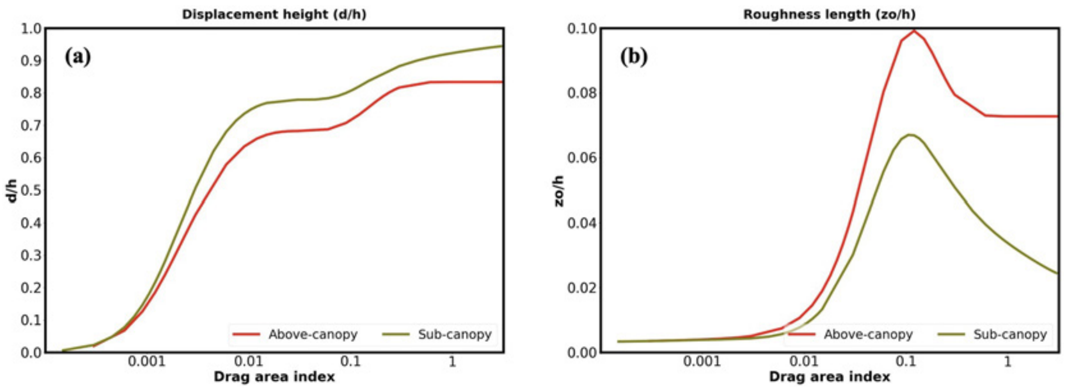

Figure A1. The dependencies of (a) $\frac{d}{h}$ and (b) $\frac{z_0}{h}$ on drag area index following the $\xi_{max} = 0.8$ configuration in Figure 5 and 6 in M17, respectively. Red and green lines are for above-canopy and sub-canopy fires, respectively.

The calculation of d and z_0 is verified following the approaches in M17 and the results are shown in Figure A1. The variations of $\frac{d}{h}$ and $\frac{z_0}{h}$ from the canopy wind model are comparable with the results shown in Figures 5 and 6 in M17, respectively. The differences in $\frac{d}{h}$ and $\frac{z_0}{h}$ may be due to different model layer resolution configurations and the use of input variable z_0 as first guess for u_c and $CTRESS$ calculation.

Appendix B: Regional NWP Modeling Application–March 2020 Case

Along with the discussion in Section 4, a case on 1 March 2020 is demonstrated as an additional example of the application of the canopy wind model. Similarly, the wind speeds (Figures B1e–B1i) are significantly reduced to less than 2 m s^{-1} over forest regions, and start to increase when heights become higher within or above the canopy top. Figure B2 is an example of the blended 10-m wind speeds at identified forest grids. Also, the low flame heights result in low WAF values and midflame wind speeds (Figure B3), as the wind speeds are significantly reduced by the forest canopy over the southeastern US.

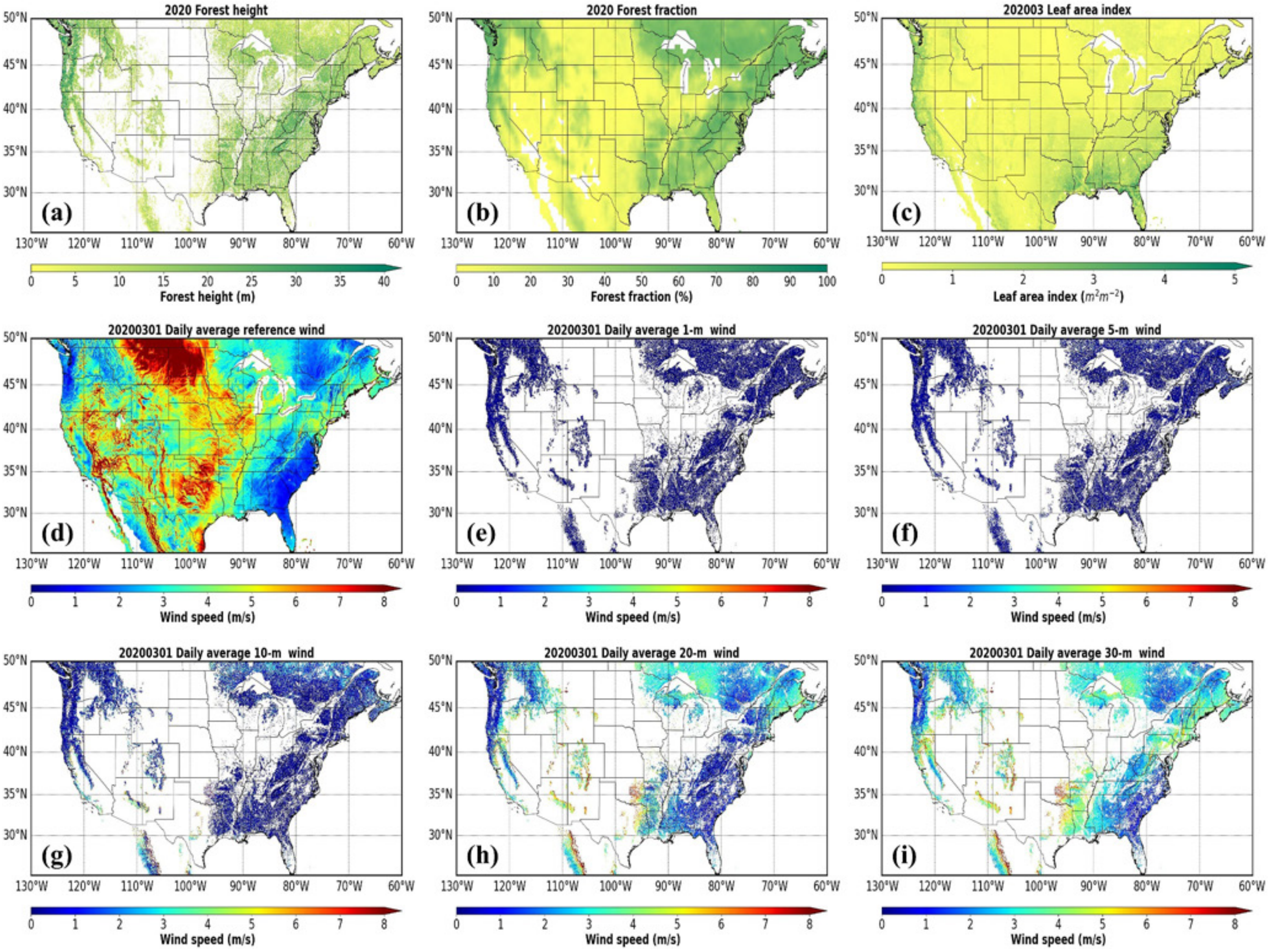

Figure B1. Same as Figure 6 but for 1 March 2020.

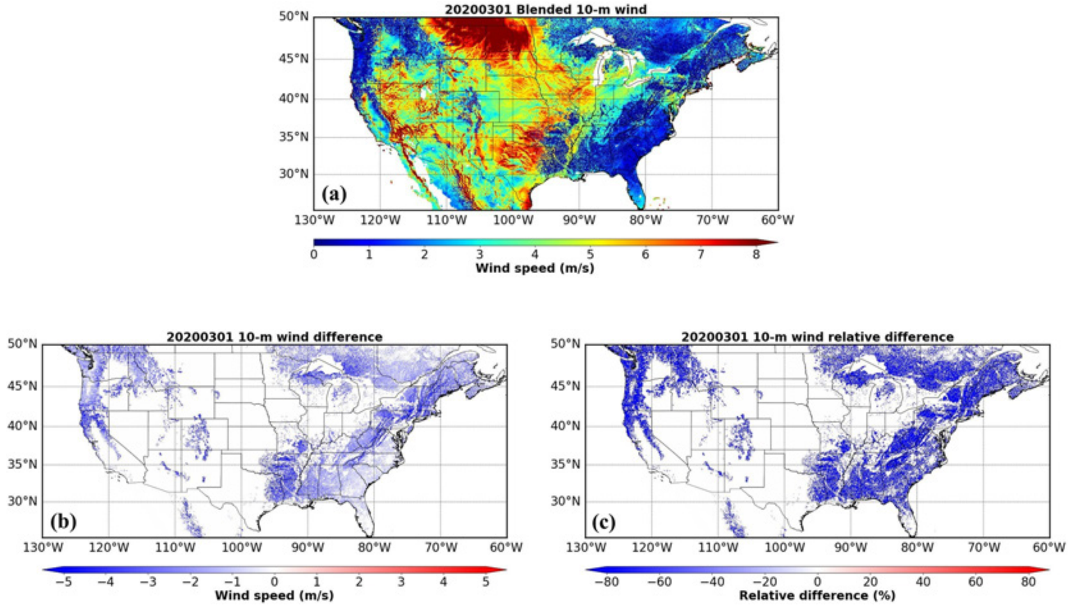

Figure B2. Same as Figure 7 but for 1 March 2020.

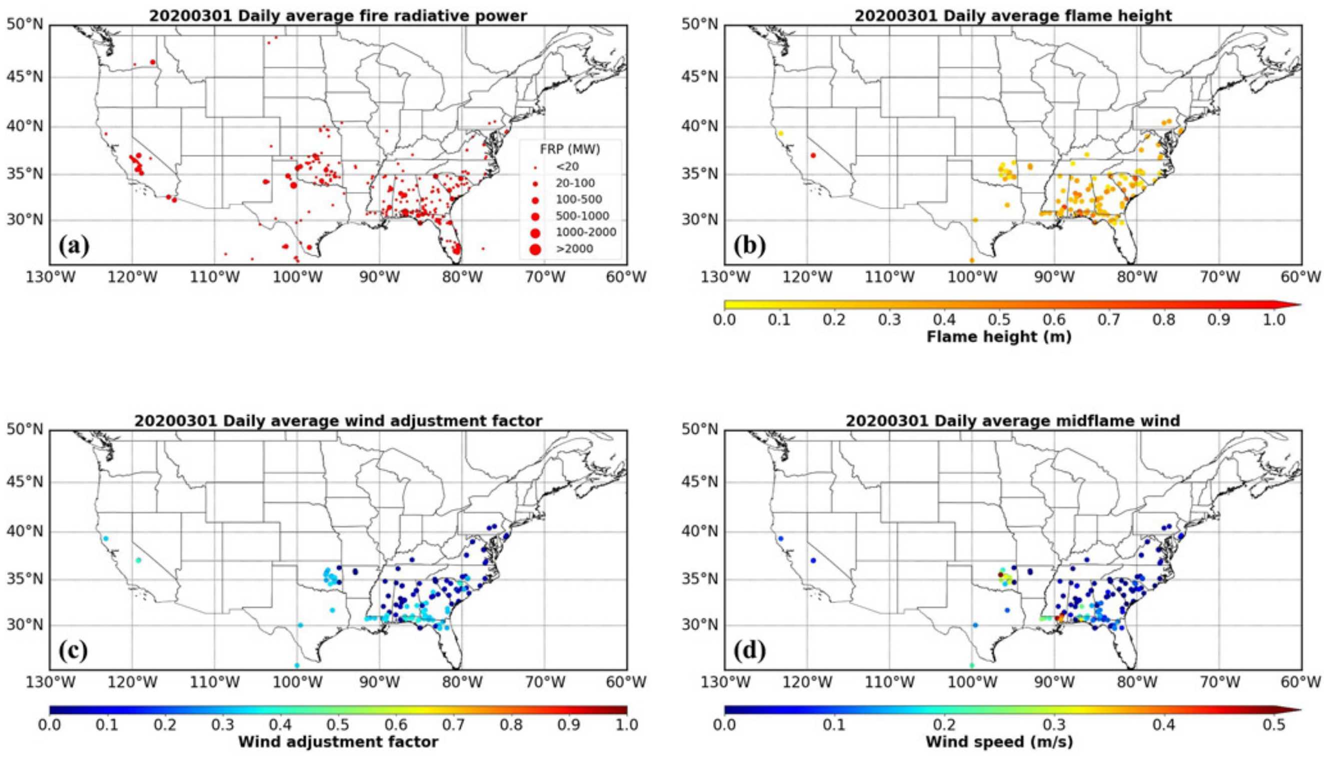

Figure B3. Same as Figure 8 but for 1 March 2020.

Appendix C: Evaluation of Wind Adjustment Factor

The calculation of WAF in the WAF model is verified following the approaches in M17. Results are shown in Figure C1.

Overall, the WAF model generally produces reasonable WAF values in general compared with Figure 9 in M17. The WAF from the WAF model shows a similar trend to Figure 12 in M17. WAF values are constrained to less than 0.1 for the sub-canopy case while they grow rapidly with flame height for the above-canopy case. A discontinuity at the canopy top (10 m) is also found, showing different characteristics for sub- and above-canopy fires. Low WAF values due to high PAI values in a dense canopy (canopy fraction = 0.8) based on both PAI options are expected; although the Katul et al. (2004) look-up table provides constant PAI values based on vegetation type only, the PAI parameterization in Equation 19 of M17 is canopy-height- and canopy-fraction-dependent. Therefore, the low PAI values in a sparse canopy (canopy fraction = 0.3) generated by M17 approach result in significantly high WAF values compared to a dense canopy. This could be a possible source of uncertainty in the WAF application.

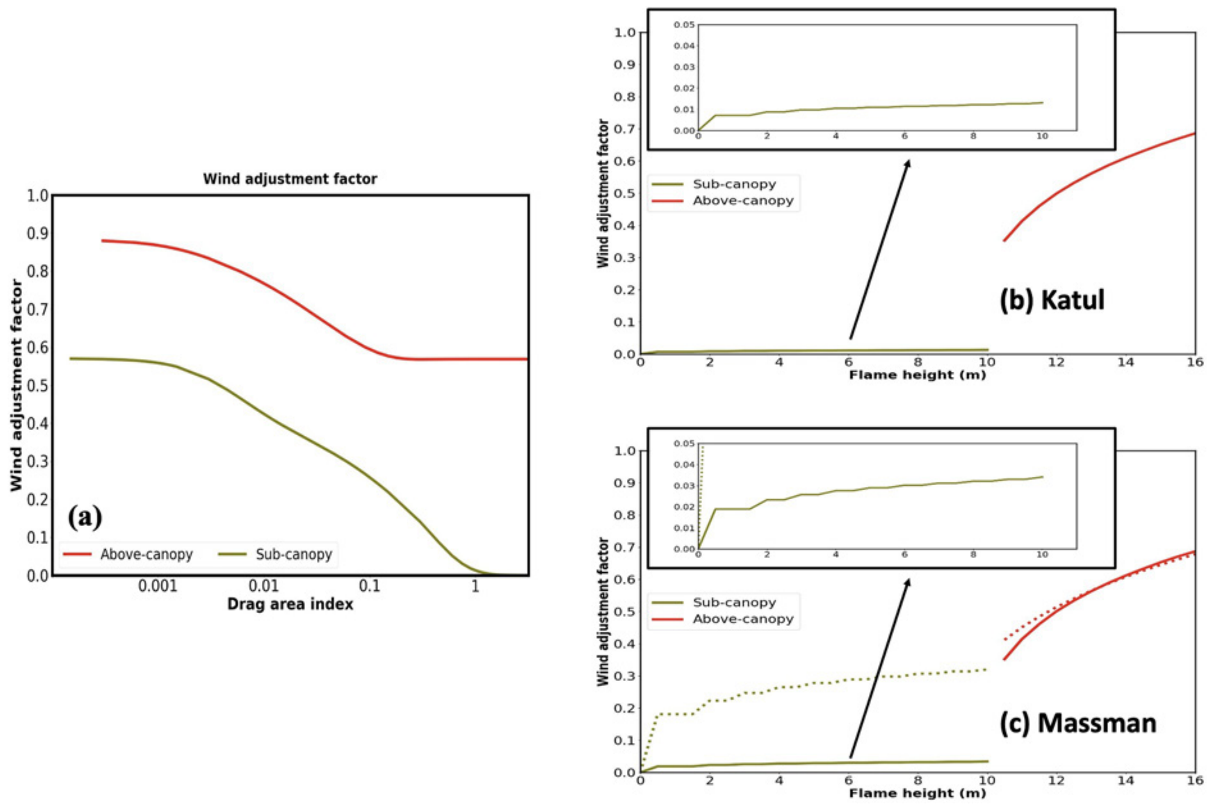

Figure C1. The dependencies of (a) wind adjustment factor (WAF) on drag area index following the $\xi_{max} = 0.8$ configuration in Figure 9 in M17. The dependencies of WAF on flame height using the (b) plant area index (PAI) look-up table from Katul et al. (2004) and (c) PAI parameterization from M17 Equation 19, with canopy height as 10 m (i.e., $h = 10$) and changing flame heights following the configuration in Figure 12 in M17. Red and green lines are for above-canopy and sub-canopy fires, respectively. In (b) and (c), solid and dashed lines are results using canopy fraction as 0.8 and 0.3, respectively. Note that the results with canopy fraction as 0.3 are same as those with canopy fraction as 0.8 when using the Katul et al. (2004) look-up table.

Appendix D: Evaluation of Rate of Spread

The ROS calculated based on the Rothermel's model is evaluated by comparing with those reported in Varga et al. (2022). In Rothermel's model, average fuel parameters of chaparral, brush, and hardwood slash are used based on Andrews (2018), and wind speeds are adapted from Table 3 in Varga et al. (2022). Results are shown in Figure D1.

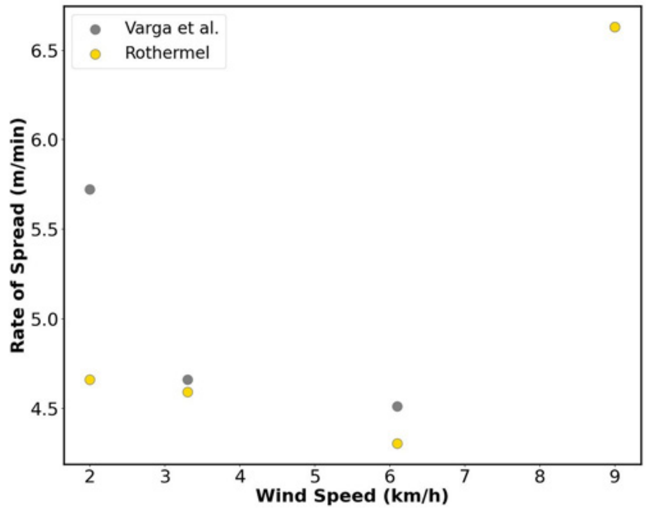

Figure D1. Comparison of the rates of spread (ROS) calculated by Rothermel's surface fire spread model and Varga et al. (2022).

Appendix E: Model Sensitivity to the RSL Influence Function

The sensitivity of the canopy wind model to the influence function λ_{rs} $(1 \le \lambda_{rs} \le 1.25)$ adopted from Massman et al. (2017) (M17), which represents the RSL effect in u_c calculation, is evaluated. The full wind profile at 0600 UTC at US-xTE site (Figures 2 and 3d) is used as the test case. All model configurations (PAI option, vegetation type, vertical layer resolution) follow the default settings described in Section 3.3. Results are shown in Figure E1 and Table E1. Overall, the canopy wind model shows nearly no sensitivity to the selection of λ_{rs}, which has a range of 1–1.25 by definition (Massman et al., 2017). Although u_c estimation increases with λ_{rs}, the impact on the wind profile estimation is relatively minor. It is probably that λ_{rs} is already a simplification and thus has small variability. The results emphasize the limitation of using λ_{rs} to represent the RSL effect which varies with weather and canopy characteristics.

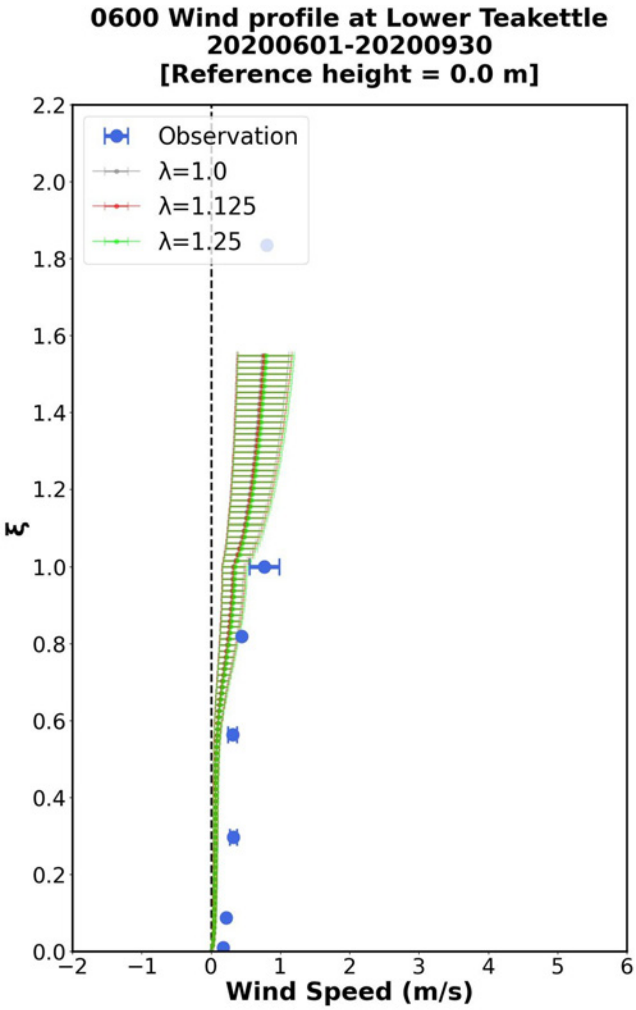

Figure E1. In-canopy section of full wind profiles with $\lambda_{rs} = 1$, 1.125 and 1.25 at Lower Teakettle site, 0600 UTC. The height where $\xi = 1$ is the canopy top. The model configuration for each run is the same except for the λ_{rs} value.

Table E1
Mean Estimated Wind Speed at the Canopy Top (u_c, m s^{-1}), and Mean Absolute Biases (m s^{-1}) and Root Mean Square Error (m s^{-1}) of Model Wind Profiles Within the Canopy ($\xi \leq 1$) Compared With Observations at US-xTE Site, 0600 UTC

λ_{rs}	u_c estimation (m s^{-1})	Mean absolute (m s^{-1})	Root mean square error (m s^{-1})
1.00	0.31 ± 0.16	−0.21 ± 0.14	0.27
1.125	0.33 ± 0.17	−0.19 ± 0.14	0.27
1.25	0.35 ± 0.18	−0.18 ± 0.14	0.26

Note. The mean u_c observation is 0.77 ± 0.21 m s^{-1}. The model configuration for each run is the same except for the λ_{rs} value.

Appendix F: Evaluation of Flame Height Estimation Option

The influence of different flame height option on the estimation of midflame wind speed is discussed. The model configurations of the results shown here are the same as those shown in Section 4.2.

Figure F1 presents the difference between the midflame wind speeds using three flame height options compared to the default FRP-dependent flame height calculation. In Figure F1a, the midflame wind speeds generally increase when setting the flame height to 2 m (i.e. the height of midflame point as 1 m), particularly for the fires in the southern US that are typically grass fires with low FRP and very low flame height. Enhanced wind speeds are expected as the user-defined flame height simply brings wind speeds to a higher altitude. However, differences of the midflame wind speeds for the forest fires in the western and southeastern US are minor (<0.5 m s^{-1}). This is because the wind speeds are significantly affected by the canopy and the midflame point at 1 m above the ground is still well within the deep canopy, resulting in significant wind speed reductions. In Figure F1b, the enhancements of midflame wind speeds are more significant by setting the flame height equal to the canopy height (i.e., midflame point locates at the center of the canopy) for fires in Idaho, Arkansas and Louisiana, which are mostly covered by savannas and grasslands. These relatively sparse and short vegetations, which are identified as above-canopy fires, showed minimal effects on the WAF calculation in the WAF model (Equation 15), leading to stronger midflame wind speeds compared to the forest regions such as California and the southeast. In Figure F1c, the midflame wind speeds using flame height with the crown fire option increased by 1–2 m s^{-1} for fires with low-lying vegetation compared to the default FRP-dependent option, while the enhancements are still minor (<0.5 m s^{-1}) for forest fires in the western US. This is probably because the difference between the in-canopy wind speeds and u_c is relatively small in the forest over this region (Figure 4). While the mid-flame wind speeds show generally minor changes after adjusting flame height from the midflame point to canopy top, they are still significantly lower compared to typical 10-m wind speeds and could influence the spread of fires.

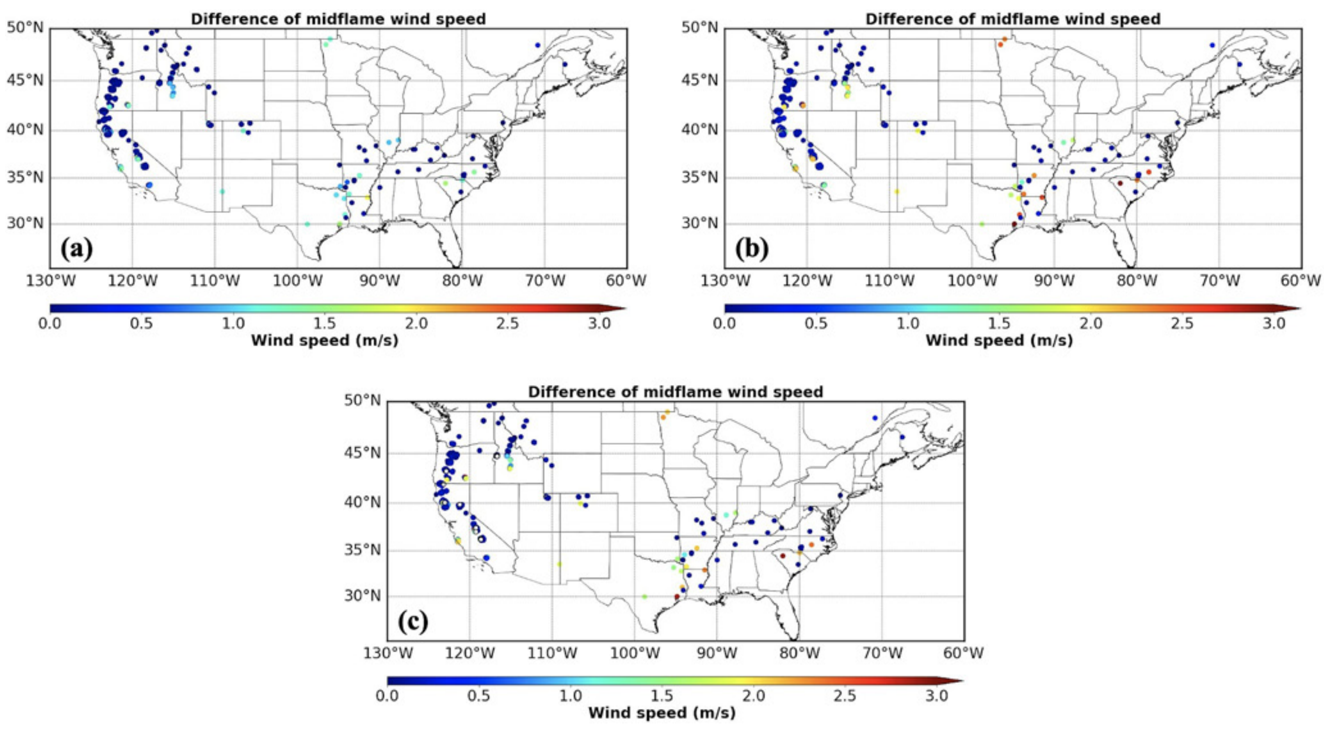

Figure F1. Difference of the midflame wind speeds using (a) a constant user-defined flame height as 2 m, (b) flame height equals to the canopy height, and (c) flame height with crown fire option compared to those using default FRP-dependent flame height. Fires that are not identified as crown fires are shown as white dots as they have no changes in midflame wind speeds.

Note that although crown fires are typically associated with forest fires (Stocks et al., 2004; Taylor et al., 2004; Wagner, 1977), fires with low-lying vegetation (e.g., grassland fires) may be identified as crown fires in the WAF model since the crown fire identification is based on fire intensity (i.e., FRP) only. Also, in WAF calculation, fire types (sub-canopy and above-canopy fires) are determined based on VIIRS AST, which only provides the dominant vegetation/canopy type and may miss the regional variation of vegetative species of a given grid. For instance, a tree crown fire could be identified as an above-canopy fire in the WAF model since it occurs over a grassland-dominated area, suggesting potential uncertainties in WAF calculation.

Data Availability Statement

The data sets used in this study are available to download from the links listed in Table 3. The source code of the canopy model set is publicly available at Campbell et al. (2024).

Acknowledgments

This study was co-funded by the UMD/NOAA/CISESS: GMU Air Surface Exchange and Atmospheric Composition Research (NOAA Sponsor Number: 79785-Z7554202 Amend A; CISESS Funding Number: NA19NES4320002) and NOAA/In-Canopy Processes Research (NOAA Sponsor Number: NA22OAR4590516) projects. We acknowledge the GoAmazon project and following AmeriFlux sites for their data records: US-Chr, US-WCr, US-xBR, and US-xTE. We acknowledge that the results and conclusions presented in this work, as well as any views expressed herein, are those of the authors and may not necessarily reflect the views of NOAA or the Department of Commerce.

References

Abolafia-Rosenzweig, R., He, C., Burns, S. P., & Chen, F. (2021). Implementation and evaluation of a unified turbulence parameterization throughout the canopy and roughness sublayer in Noah-MP snow simulations. *Journal of Advances in Modeling Earth Systems*, *13*(11), e2021MS002665. https://doi.org/10.1029/2021MS002665

Ahmadov, R., Grell, G., James, E., Csiszar, I., Tsidulko, M., Pierce, B., et al. (2017). Using VIIRS fire radiative power data to simulate biomass burning emissions, plume rise and smoke transport in a real-time air quality modeling system. In *IEEE International Geoscience and Remote Sensing Symposium (IGARSS)* (pp. 2806–2808). https://doi.org/10.1109/IGARSS.2017.8127581

Albini, F. A., Alexander, M. E., & Cruz, M. G. (2012). A mathematical model for predicting the maximum potential spotting distance from a crown fire. *International Journal of Wildland Fire*, *21*(5), 609. https://doi.org/10.1071/wf11020

Alexander, C. R., Weygandt, S. S., Smirnova, T. G., Benjamin, S., Hofmann, P., James, E. P., & Koch, D. A. (2010). High Resolution Rapid Refresh (HRRR): Recent enhancements and evaluation during the 2010 convective season. In *Preprints, 25th Conf. On severe local storms* (Vol. 9.2). Amer. Meteor. Soc. Retrieved from https://ams.confex.com/ams/pdfpapers/175722.pdf

Alexander, M. E. (1982). Calculating and interpreting forest fire intensities. *Canadian Journal of Botany*, *60*(4), 349–357. https://doi.org/10.1139/b82-048

Alexander, M. E., & Cruz, M. G. (2011). Crown fire dynamics in conifer forests. In P. Werth, B. Potter, C. Clements, M. Finney, S. Goodrick, M. Alexander, et al. (Eds.), *Synthesis of knowledge of extreme fire behavior* (Vol. 1, pp. 107–142). Retrieved from https://www.firescience.gov/projects/09-S-03-1/project/09-S-03-1_AlexanderCruz_2011_PNW_GTR854_Chpt8.pdf

Alexander, M. E., & Cruz, M. G. (2012). Interdependencies between flame length and fireline intensity in predicting crown fire initiation and crown scorch height. *International Journal of Wildland Fire*, *21*(2), 95. https://doi.org/10.1071/wf11001

Anderson, H. E., Brackebusch, A. P., Mutch, R. W., & Rothermel, R. C. (1966). Mechan-isms of fire spread research progress report 2. In *USDA forest service, intermountain forest and range experiment station, research paper INT-28*.

Andreae, M. O., & Merlet, P. (2001). Emission of trace gases and aerosols from biomass burning. *Global Biogeochemical Cycles*, *15*(4), 955–966. https://doi.org/10.1029/2000GB001382

Andrews, P. L. (2012). Modeling wind adjustment factor and midflame wind speed for Rothermel's surface fire spread model. In *General technical reports RMRS-GTR-266*. U.S. Department of Agriculture, Forest Service, Rocky Mountain Research Station. https://doi.org/10.2737/RMRS-GTR-266

Andrews, P. L. (2018). The Rothermel surface fire spread model and associated developments: A comprehensive explanation. In *General technical reports RMRS-GTR-371*. U.S. Department of Agriculture, Forest Service, Rocky Mountain Research Station. 121. https://doi.org/10.2737/RMRS-GTR-371

Andrews, P. L., Heinsch, F. A., & Schelvan, L. (2011). *How to generate and interpret fire characteristics charts for surface and crown fire behavior. General Technical Reports RMRS-GTR-253*. U.S. Department of Agriculture, Forest Service, Rocky Mountain Research Station. https://doi.org/10.2737/RMRS-GTR-253

Bai, H., & Schumacher, C. (2020). The interaction between the Nocturnal Amazonian Low-level jet and convection in CESM. *Journal of Climate*, *34*(21), 8519–8532. https://doi.org/10.1175/JCLI-D-21-0042.1

Beer, T. (1993). The speed of a fire front and its dependence on wind-speed. *International Journal of Wildland Fire*, *3*(4), 193. https://doi.org/10.1071/wf9930193

Bonan, G. B., Patton, E. G., Harman, I. N., Oleson, K. W., Finnigan, J. J., Lu, Y., & Burakowski, E. A. (2018). Modeling canopy-induced turbulence in the Earth system: A unified parameterization of turbulent exchange within plant canopies and the roughness sublayer (CLM-ml v0). *Geoscientific Model Development*, *11*(4), 1467–1496. https://doi.org/10.5194/gmd-11-1467-2018

Boudreault, L.-É., Bechmann, A., Sørensen, N. N., Sogachev, A., & Dellwik, E. (2014). Canopy structure effects on the wind at a complex forested site. *Journal of Physics: Conference Series*, *524*, 012112. https://doi.org/10.1088/1742-6596/524/1/012112

Burrows, N. D. (1994). Experimental development of a fire management model for jarrah (Eucalyptus marginata Donn ex Sm.) forest PhD thesis. *Australian National University, Canberra*. https://doi.org/10.25911/5d78d89a1d6c0

Byram, G. M. (1959). Combustion of forest fuels. In K. P. Davis (Ed.), *Forest fire: Control and use*. McGraw Hill.

Campbell, P., Moon, Z., Hung, W.-T., & Rasool, Q. A. (2024). Noaa-oar-arl/canopy-app: Canopy wind paper v2 (canopy-wind-paper-v2) [Software]. *Zenodo*. https://doi.org/10.5281/zenodo.10553373

Catchpole, W. R., Bradstock, R. A., Choate, J., Fogarty, L. G., Gellie, N., McCarthy, G., et al. (1998). Cooperative development of equations for heathland fire behaviour. In *Proceedings of 3rd international conference on forest fire research and 14th conference on fire and forest meteorology, volume II", 16–20 November 1998, Luso–Coimbra, Portugal*.

Chen, J., Franklin, J. F., & Spies, T. A. (1993). Contrasting microclimates among clearcut, edge, and interior of old-growth Douglas-fir forest. *Agricultural and Forest Meteorology*, *63*(3–4), 219–237. https://doi.org/10.1016/0168-1923(93)90061-l

Chen, J. M., & Cihlar, J. (1995). Plant canopy gap-size analysis theory for improving optical measurements of leaf-area index. *Applied Optics*, *34*(27), 6211–6222. https://doi.org/10.1364/AO.34.006211

Chen, J. M., Rich, P. M., Gower, S. T., Norman, J. M., & Plummer, S. (1997). Leaf area index of boreal forests: Theory, techniques, and measurements. *Journal of Geophysical Research*, *102*(D24), 29429–29443. https://doi.org/10.1029/97JD01107

Cheney, N. P., & Gould, J. S. (1995). Fire growth in grassland fuels. *International Journal of Wildland Fire*, *5*(4), 237–247. https://doi.org/10.1071/WF9950237

Cheney, N. P., Gould, J. S., & Catchpole, W. R. (1993). The influence of fuel, weather and fire shape variables on fire-spread in grasslands. *International Journal of Wildland Fire*, *3*(1), 31–44. https://doi.org/10.1071/WF9930031

Cheney, N. P., Gould, J. S., & Catchpole, W. R. (1998). Prediction of fire spread in grasslands. *International Journal of Wildland Fire*, *8*, 1–13. https://doi.org/10.1071/WF9980001

Clark, R. G. (1983). *Threshold requirements for fire spread in grassland fuels*. PhD dissertation. Texas Tech University.

Coen, J. L., Cameron, M., Michalakes, J., Patton, E. G., Riggan, P. J., & Yedinak, K. M. (2013). WRF-Fire: Coupled weather–wildland fire modeling with the weather research and forecasting model. *Journal of Applied Meteorology and Climatology*, *52*(1), 16–38. https://doi.org/10.1175/JAMC-D-12-023.1

Crutzen, P. J., & Andreae, M. O. (1990). Biomass burning in the tropics: Impact on atmospheric chemistry and biogeochemical cycles. *Science*, *250*(4988), 1669–1678. https://doi.org/10.1126/science.250.4988.1669

Dhargay, S., Lyell, C. S., Brown, T. P., Inbar, A., Sheridan, G. J., & Lane, P. N. J. (2022). Performance of GEDI space-borne LiDAR for quantifying structural variation in the temperate forests of South-Eastern Australia. *Remote Sensing*, *14*(15), 3615. https://doi.org/10.3390/rs14153615

DiMiceli, C., Sohlberg, R., & Townshend, J. (2022). MODIS/Terra vegetation continuous fields yearly L3 global 250m SIN grid V061 [Dataset]. *NASA EOSDIS Land Processes DAAC*. https://doi.org/10.5067/MODIS/MOD44B.061

Dowell, D. C., Alexander, C. R., James, E. P., Weygandt, S. S., Benjamin, S. G., Manikin, G. S., et al. (2022). The High-Resolution Rapid Refresh (HRRR): An hourly updating convection-allowing forecast model. Part I: Motivation and system description. *Weather and Forecasting*, *37*(8), 1371–1395. https://doi.org/10.1175/WAF-D-21-0151.1

Dubayah, R., Tang, H., Armston, J., Luthcke, S., Hofton, M., & Blair, J. (2021). GEDI L2B canopy cover and vertical profile metrics data global footprint level V002 [Dataset]. *NASA EOSDIS Land Processes DAAC*. https://doi.org/10.5067/GEDI/GEDI02_B.002

Eftekharian, E., Ghodrat, M., He, Y., Ong, R. H., Kwok, K. C. S., & Zhao, M. (2019b). Numerical analysis of the effect of fire source configuration on fire-wind enhancement. *Heat Transfer Engineering*, *42*(1), 41–60. https://doi.org/10.1080/01457632.2019.1685249

Eftekharian, E., Ghodrat, M., He, Y., Ong, R. H., Kwok, K. C. S., Zhao, M., & Samali, B. (2019a). Investigation of terrain slope effects on wind enhancement by a line source fire. *Case Studies in Thermal Engineering*, *14*, 100467. https://doi.org/10.1016/j.csite.2019.100467

Eftekharian, E., Ghodrat, M., Ong, R. H., He, Y., & Kwok, K. C. S. (2018). CFD investigation of cross-flow effects on fire-wind enhancement. In *Proceedings of the 21St Australasian fluid mechanics conference, 10-13 December 2018*. Retrieved from https://people.eng.unimelb.edu.au/imarusic/proceedings/21%20AFMC%20TOC.html

Eftekharian, E., Salehi, F., He, Y., & Kwok, K. C. S. (2021). LES analysis of fire source aspect ratio effects on fire-wind enhancement. *International Journal of Heat and Fluid Flow*, *89*, 108803. https://doi.org/10.1016/j.ijheatfluidflow.2021.108803

Ek, M. B., Mitchell, K. E., Lin, Y., Rogers, E., Grunmann, P., Koren, V., et al. (2003). Implementation of Noah land surface model advances in the National Centers for Environmental Prediction operational mesoscale Eta model. *Journal of Geophysical Research*, *108*, 8851. https://doi.org/10.1029/2002JD003296,D22

Fang, H., Baret, F., Plummer, S., & Schaepman-Strub, G. (2019). An overview of global Leaf Area Index (LAI): Methods, products, validation, and applications. *Reviews of Geophysics*, *57*(3), 739–799. https://doi.org/10.1029/2018RG000608

Fernandes, P. M., Botelho, H. S., Rego, F. C., & Loureiro, C. (2009). Empirical modelling of surface fire behaviour in maritime pine stands. *International Journal of Wildland Fire*, *18*(6), 698–710. https://doi.org/10.1071/WF08023

Fernandes, P. M., Catchpole, W. R., & Rego, F. C. (2000). Shrubland fire behaviour modelling with microplot data. *Canadian Journal of Forest Research*, *30*(6), 889–899. https://doi.org/10.1139/X00-012

Forestry Canada Fire Danger Group. (1992). Development of the Canadian forest fire behavior prediction system, information report ST-X-3. In *Canadian forest service publications: Sault Ste. Marie, ON* (Vol. 3).66

Freire, L. S., Gerken, T., Ruiz-Plancarte, J., Wei, D., Fuentes, J. D., Katul, G. G., et al. (2017). Turbulent mixing and removal of ozone within an Amazon rainforest canopy. *Journal of Geophysical Research: Atmospheres*, *122*(5), 2791–2811. https://doi.org/10.1002/2016JD026009

Fuentes, J. D., Chamecki, M., Nascimento dos Santos, R. M., von Randow, C., Stoy, P. C., Katul, G., et al. (2016). Linking meteorology, Turbulence, and air chemistry in the Amazon rain forest. *Bulletin of the American Meteorological Society*, *97*(12), 2329–2342. https://doi.org/10.1175/BAMS-D-15-00152.1

Gower, S. T., Kucharik, C. J., & Norman, J. M. (1999). Direct and indirect estimation of leaf area index, fAPAR, and net primary production of terrestrial ecosystems. *Remote Sensing of Environment*, *70*(1), 29–51. https://doi.org/10.1016/S0034-4257(99)00056-5

Grimmond, C. S. B., Robeson, S. M., & Schoof, J. T. (2000). Spatial variability of micro-climatic conditions within a mid-latitude deciduous forest. *Climate Research*, *15*(2), 137–149. https://doi.org/10.3354/cr015137

Harman, I. N., & Finnigan, J. J. (2007). A simple unified theory for flow in the canopy and roughness sublayer. *Boundary-Layer Meteorology*, *123*(2), 339–363. https://doi.org/10.1007/s10546-006-9145-6

Harman, I. N., & Finnigan, J. J. (2008). Scalar concentration profiles in the canopy and roughness sublayer. *Boundary-Layer Meteorology*, *129*(3), 323–351. https://doi.org/10.1007/s10546-008-9328-4

He, C., Valayamkunnath, P., Barlage, M., Chen, F., Gochis, D., Cabell, R., et al. (2023). Modernizing the open-source community Noah-MP land surface model (version 5.0) with enhanced modularity, interoperability, and applicability. *EGUsphere*, *16*, 5131–5151. https://doi.org/10.5194/egusphere-2023-675

Huang, C., Zhan, X., & Csiszar, I. (2022). Algorithm theoretical basis document for NOAA VIIRS surface type. Sep. 2022. https://www.star.nesdis.noaa.gov/jpss/documents/ATBD/ATBD_VIIRS-SurfaceType_v2.1.pdf

Katul, G. G., Mahrt, L., Poggi, D., & Sanz, C. (2004). ONE- and TWO-equation models for canopy turbulence. *Boundary-Layer Meteorology*, *113*(1), 81–109. https://doi.org/10.1023/B:BOUN.0000037333.48760.e5

Kaulfus, A. S., Nair, U., Jaffe, D., Christopher, S. A., & Goodrick, S. (2017). Biomass burning smoke climatology of the United States: Implications for particulate matter air quality. *Environmental Science & Technology*, *51*(20), 11731–11741. https://doi.org/10.1021/acs.est.7b03292

Koo, E., Pagni, P. J., Weise, D. R., & Woycheese, J. P. (2010). Firebrands and spotting ignition in large-scale fires. *International Journal of Wildland Fire*, *19*(7), 818. https://doi.org/10.1071/wf07119

Kucharik, C. J., Norman, J. M., & Gower, S. T. (1998). Measurements of branch area and adjusting leaf area index indirect measurements. *Agricultural and Forest Meteorology*, *91*(1–2), 69–88. https://doi.org/10.1016/S0168-1923(98)00064-1

Lamaud, E., Carrara, A., Brunet, Y., Lopez, A., & Druilhet, A. (2002). Ozone fluxes above and within a pine forest canopy in dry and wet conditions. *Atmospheric Environment*, *36*(1), 77–88. https://doi.org/10.1016/S1352-2310(01)00468-X

Lawrence, D. M., Fisher, R. A., Koven, C. D., Oleson, K. W., Swenson, S. C., Bonan, G., et al. (2019). The Community Land Model version 5: Description of new features, benchmarking, and impact of forcing uncertainty. *Journal of Advances in Modeling Earth Systems*, *11*(12), 4245–4287. https://doi.org/10.1029/2018MS001583

Li, F., Zhang, X., Kondragunta, S., Lu, X., Csiszar, I., & Schmidt, C. C. (2022). Hourly biomass burning emissions product from blended geostationary and polar-orbiting satellites for air quality forecasting applications. *Remote Sensing of Environment*, *281*, 133237. https://doi.org/10.1016/j.rse.2022.113237

Li, Z., Strahler, A., Schaaf, C., Jupp, D., Schaefer, M., & Olofsson, P. (2018). Seasonal change of leaf and woody area profiles in a midlatitude deciduous forest canopy from classified dual-wavelength terrestrial LIDAR point clouds. *Agricultural and Forest Meteorology*, *262*, 279–297. https://doi.org/10.1016/j.agrformet.2018.07.014

Linn, R. R., & Cunningham, P. (2005). Numerical simulations of grass fires using a coupled atmosphere–fire model: Basic fire behavior and dependence on wind speed. *Journal of Geophysical Research*, *110*(D13), D13107. https://doi.org/10.1029/2004JD005597

Liu, N., Lei, J., Gao, W., Chen, H., & Xie, X. (2021). Combustion dynamics of large-scale wildfires. *Proceedings of the Combustion Institute*, *38*(1), 157–198. https://doi.org/10.1016/j.proci.2020.11.006

Makar, P. A., Staebler, R. M., Akingunola, A., Zhang, J., McLinden, C., Karol, S. K., et al. (2017). The effects of forest canopy shading and turbulence on boundary layer ozone. *Nature Communications*, *8*(1), 15243. https://doi.org/10.1038/ncomms15243

Mallia, D. V., Kochanski, A. K., Urbanski, S. P., Mandel, J., Farguell, A., & Krueger, S. K. (2020). Incorporating a canopy parameterization within a coupled fire-atmosphere model to improve a smoke simulation for a prescribed burn. *Atmosphere*, *11*(8), 832. https://doi.org/10.3390/atmos11080832

Martano, P. (2000). Estimation of surface roughness length and displacement height from single-level sonic anemometer data. *Journal of Applied Meteorology*, *39*(5), 708–715. https://doi.org/10.1175/1520-0450(2000)039<0708:eosrla>2.0.co;2

Massman, W. J., Forthofer, J. M., & Finney, M. A. (2017). An improved canopy wind model for predicting wind adjustment factors and wildland fire behavior. *Canadian Journal of Forest Research*, *47*(5), 594–603. https://doi.org/10.1139/cjfr-2016-0354

Monin, A. S., & Obukhov, A. M. (1954). Basic laws of turbulent mixing in the surface layer of the atmosphere. *Contributions of the Geophysical Institute of the Slovak Academy of Sciences USSR*, *24*, 163–187.

Myneni, R., & Knyazikhin, Y. (2018). VIIRS/NPP leaf area index/FPAR 8-Day L4 global 500m SIN grid V001 [Dataset]. *NASA EOSDIS Land Processes DAAC*. https://doi.org/10.5067/VIIRS/VNP15A2H.001

Nelson Jr, R. M., & Adkins, C. W. (1986). Flame characteristics of wind-driven surface fires. *Canadian Journal of Forest Research*, *16*(6), 1293–1300. https://doi.org/10.1139/X86-229

Nelson Jr, R. M. (1980). Flame characteristics for fires in southern fuels. In *USDA forest service, southeastern forest experiment station, research paper SE-205*.

Niu, G. Y., Yang, Z. L., Mitchell, K. E., Chen, F., Ek, M. B., Barlage, M., et al. (2011). The community Noah land surface model with multiparameterization options (Noah-MP): 1. Model description and evaluation with local-scale measurements. *Journal of Geophysical Research*, *116*(D12), D12109. https://doi.org/10.1029/2010JD015139

Olivas, P. C., Oberbauer, S. F., Clark, D. B., Clark, D. A., Ryan, M. G., O'Brien, J. J., & Ordoñez, H. (2013). Comparison of direct and indirect methods for assessing leaf area index across a tropical rain forest landscape. *Agricultural and Forest Meteorology*, *177*, 110–116. https://doi.org/10.1016/j.agrformet.2013.04.010

Physick, W. L., & Garratt, J. R. (1995). Incorporation of a high-roughness lower boundary into a mesoscale model for studies of dry deposition over complex terrain. *Boundary-Layer Meteorology*, *74*(1–2), 55–71. https://doi.org/10.1007/bf00715710

Poggi, D., Porporato, A., Ridolfi, L., Albertson, J. D., & Katul, G. G. (2004). The effect of vegetation density on canopy sub-layer turbulence. *Boundary-Layer Meteorology*, *111*(3), 565–587. https://doi.org/10.1023/b:boun.0000016576.05621.73

Potapov, P., Hansen, M. C., Pickens, A., Hernandez-Serna, A., Tyukavina, A., Turubanova, S., et al. (2022). The global 2000-2020 land cover and land use change dataset derived from the Landsat archive: First results. *Frontiers in Remote Sensing*, *3*. https://doi.org/10.3389/frsen.2022.856903

Potapov, P., Li, X., Hernandez-Serna, A., Tyukavina, A., Hansen, M. C., Kommareddy, A., et al. (2020). Mapping and monitoring global forest canopy height through integration of GEDI and Landsat data. *Remote Sensing of Environment*, *253*, 112165. https://doi.org/10.1016/j.rse.2020.112165

Raupach, M. R. (1991). Vegetation-atmosphere interaction in homogeneous and heterogeneous terrain: Some implications of mixed-layer dynamics. *Vegetatio*, *91*(1/2), 105–120. https://doi.org/10.1007/bf00036051

Raupach, M. R., Finnigan, J. J., & Brunei, Y. (1996). Coherent eddies and turbulence in vegetation canopies: The mixing-layer analogy. *Boundary-Layer Meteorology*, *78*(3–4), 351–382. https://doi.org/10.1007/bf00120941

Raupach, M. R., & Thom, A. S. (1981). Turbulence in and above plant canopies. *Annual Review of Fluid Mechanics*, *13*(1), 97–129. https://doi.org/10.1146/annurev.fl.13.010181.000525

Reid, J. S., Koppmann, R., Eck, T. F., & Eleuterio, D. P. (2005). A review of biomass burning emissions part II: Intensive physical properties of biomass burning particles. *Atmospheric Chemistry and Physics*, *5*(3), 799–825. https://doi.org/10.5194/acp-5-799-2005

Rothermel, R. C. (1972). A mathematical model for predicting fire spread in wildland fuels. In *Res. Pap. INT-115. Ogden, UT: U.S. Department of agriculture. Intermountain forest and range experiment station*.40

Santos, D. M., Acevedo, O. C., Chamecki, M., Fuentes, J. D., Gerken, T., & Stoy, P. C. (2016). Temporal scales of the nocturnal flow within and above a forest canopy in Amazonia. *Boundary-Layer Meteorology*, *161*(1), 73–98. https://doi.org/10.1007/s10546-016-0158-5

Shapkalijevski, M. M., Moene, A. F., Ouwersloot, H. G., Patton, E. G., & Vilà-Guerau de Arellano, J. (2016). Influence of canopy seasonal changes on turbulence parameterization within the roughness sublayer over an Orchard canopy. *Journal of Applied Meteorology and Climatology*, *55*(6), 1391–1407. https://doi.org/10.1175/JAMC-D-15-0205.1

Shapkalijevski, M. M., Ouwersloot, H. G., Moene, A. F., & Arrellano, J. V. G. D. (2017). Integrating canopy and large-scale effects in the convective boundary-layer dynamics during the CHATS experiment. *Atmospheric Chemistry and Physics*, *17*(3), 1623–1640. https://doi.org/10.5194/acp-17-1623-2017

Shaw, R. H. (1977). Secondary wind speed maxima inside plant canopies. *Journal of Applied Meteorology and Climatology*, *16*(5), 514–521. https://doi.org/10.1175/1520-0450(1977)016<0514:SWSMIP>2.0.CO;2

Skamarock, W. C., Klemp, J. B., Dudhia, J., Gill, D. O., Liu, Z., Berner, J., et al. (2019). A description of the advanced research WRF version 4. *NCAR Tech. Note NCAR/TN-556+STR*, 145. https://doi.org/10.5065/1dfh-6p97

Stocks, B. J., Alexander, M. E., Wotton, B. M., Stefner, C. N., Flannigan, M. D., Taylor, S. W., et al. (2004). Crown fire behaviour in a northern jack pine-black spruce forest. *Canadian Journal of Forest Research*, *34*(8), 1548–1560. https://doi.org/10.1139/x04-054

Stull, R. B. (1988). *An introduction to boundary layer meteorology* (Vol. 13). Kluwer Academic Publishers, the Netherlands, Dor-drecht/Boston/London.

Sutherland, D., Rashid, M. A., Hilton, J. E., & Moinuddin, K. A. M. (2023). Implementation of spatially-varying wind adjustment factor for wildfire simulations. *Environmental Modelling & Software*, *163*, 105660. https://doi.org/10.1016/j.envsoft.2023.105660

Tang, H., Brolly, M., Zhao, F., Strahler, A. H., Schaaf, C. L., Ganguly, S., et al. (2014). Deriving and validating Leaf Area Index (LAI) at multiple spatial scales through lidar remote sensing: A case study in Sierra National Forest, CA. *Remote Sensing of Environment*, *143*(5), 131–141. https://doi.org/10.1016/j.rse.2013.12.007

Taylor, S. W., Wotton, B. M., Alexander, M. E., & Dalrymple, G. N. (2004). Variation in wind and crown fire behaviour in a northern jack pine-black spruce forest. *Canadian Journal of Forest Research*, *34*(8), 1561–1576. https://doi.org/10.1139/x04-116

Thom, A. S. (1971). Momentum absorption by vegetation. *Quarterly Journal of the Royal Meteorological Society*, *97*, 414–428. https://doi.org/10.1002/qj.49709741404

Thonicke, K., Spessa, A., Prentice, I. C., Harrison, S. P., Dong, L., & Carmona-Moreno, C. (2010). The influence of vegetation, fire spread and fire behaviour on biomass burning and trace gas emissions: Results from a process-based model. *Biogeosciences*, *7*(6), 1991–2011. https://doi.org/10.5194/bg-7-1991-2010

van Wilgen, B. W. (1986). A simple relationship for estimating the intensity of fires in natural vegetation. *South African Journal of Botany*, *52*(4), 384–385. https://doi.org/10.1016/S0254-6299(16)31540-X

Varga, K., Jones, C., Trugman, A., Carvalho, L. M. V., McLoughlin, N., Seto, D., et al. (2022). Megafires in a warming World: What wildfire risk factors led to California's largest recorded wildfire. *Fire*, *5*(1), 16. https://doi.org/10.3390/fire5010016

Vega, J. A., Cuinas, P., Fonturbel, T., Perez-Gorostiaga, P., & Fernandez, C. (1998). Predicting fire behaviour in Galician (NW Spain) shrubland fuel complexes. In D. X. Viegas (Ed.), *Proceedings of 3rd international conference on forest fire research and 14th conference on fire and forest meteorology, volume II", 16–20 november 1998, Luso–Coimbra, Portugal* (pp. 713–728).

Wagner, C. E. V. (1977). Conditions for the start and spread of crown fire. *Canadian Journal of Forest Research*, *7*(1), 23–34. https://doi.org/10.1139/x77-004

Wang, C., Jia, D., Lei, S., Numata, I., & Tian, L. (2023). Accuracy assessment and impact factor analysis of GEDI leaf area index product in temperate forest. *Remote Sensing*, *15*(6), 1535. https://doi.org/10.3390/rs15061535

Wang, Y., Fang, H., Zhang, Y., Li, S., Pang, Y., Ma, T., & Li, Y. (2023). Retrieval and validation of vertical LAI profile derived from airborne and spaceborne LiDAR data at a deciduous needleleaf forest site. *GIScience and Remote Sensing*, *60*, 1. https://doi.org/10.1080/15481603.2023.2214987

Weise, D. R., & Biging, G. S. (1996). Effects of wind velocity and slope on flame properties. *Canadian Journal of Forest Research*, *26*(10), 1849–1858. https://doi.org/10.1139/X26-210

Xiao, Z., Liang, S., Wang, T., & Jiang, B. (2016). Retrieval of Leaf Area Index (LAI) and Fraction of Absorbed Photosynthetically Active Radiation (FAPAR) from VIIRS time-Series data. *Remote Sensing*, *8*(4), 351. https://doi.org/10.3390/rs8040351

Xu, B., Park, T., Yan, K., Chen, C., Zeng, Y., Song, W., et al. (2018). Analysis of global LAI/FPAR products from VIIRS and MODIS sensors for spatio-temporal consistency and uncertainty from 2012–2016. *Forests*, *9*(2), 73. https://doi.org/10.3390/f9020073

Yan, K., Park, T., Chen, C., Xu, B., Song, W., Yang, B., et al. (2018). Generating global products of LAI and FPAR from SNPP-VIIRS data: Theoretical background and implementation. *IEEE Transactions on Geoscience and Remote Sensing*, *56*(4), 2119–2137. https://doi.org/10.1109/tgrs.2017.2775247

Zhang, L., Montuoro, R., McKeen, S. A., Baker, B., Bhattacharjee, P. S., Grell, G. A., et al. (2022). Development and evaluation of the aerosol forecast member in the national Center for Environment Prediction (NCEP)'s Global Ensemble Forecast System (GEFS-Aerosols v1). *Geoscientific Model Development*, *15*(13), 5337–5369. https://doi.org/10.5194/gmd-15-5337-2022

Zou, J., Yan, G., Zhu, L., & Zhang, W. (2009). Woody-to-total area ratio determination with a multispectral canopy imager. *Tree Physiology*, *29*(8), 1069–1080. https://doi.org/10.1093/treephys/tpp042

Zou, Y., Wang, Y., Ke, Z., Tian, H., Yang, J., & Liu, Y. (2019). Development of a REgion-specific ecosystem feedback fire (RESFire) model in the community Earth system model. *Journal of Advances in Modeling Earth Systems*, *11*(2), 417–445. https://doi.org/10.1029/2018MS001368

Zylstra, P. (2021). Linking fire behaviour and its ecological effects to plant traits, using FRaME in R. *Methods in Ecology and Evolution*, *12*(8), 1365–1378. https://doi.org/10.1111/2041-210X.13615